High-pressure serpentinization and abiotic methane formation in metaperidotite from the Appalachian subduction, northern Vermont

High-pressure serpentinization and abiotic methanogenesis in metaperidotite from the Appalachian subduction, northern Vermont

Antoine Boutier[1,2]*, Alberto Vitale Brovarone[1,3,4], Isabelle Martinez[2], Olivier Sissmann[5], Sara Mana[6]

[1]*Dipartimento di Scienze della Terra, Università degli Studi di Torino, Via Valperga Caluso 35, Torino, Italy*

[2]*Université de Paris, Institut de physique du globe de Paris, CNRS, F-75005 Paris, France*

[3]*Dipartimento di Scienze Biologiche, Geologiche e Ambientali, Alma Mater Studiorum Università di Bologna. Piazza di Porta San Donato 1, Bologna, Italy*

[4]*Institut de Minéralogie, de Physique des Matériaux et de Cosmochimie (IMPMC), Sorbonne Université, Muséum National d'Histoire Naturelle, UMR CNRS 7590, IRD UR206, 75005 Paris, France*

[5]*IFP Energies Nouvelles, 92500 Rueil-Malmaison, France*

[6]*Department of Geological Sciences, Salem State University, Salem, MA 01970, USA*

*Corresponding author: antoine.boutier@unito.it

Abstract

Serpentinization is the process of hydroxylation of olivine-rich ultramafic rocks to produce minerals such as serpentine, brucite and magnetite. This process is commonly accompanied by Fe oxidation and release of H_2, which can be involved in abiotic reaction pathways leading to the genesis of abiotic light hydrocarbons such as methane (CH_4). Examples of this phenomenon exist at the seafloor, such as at the serpentinite-hosted Lost City hydrothermal field, and on land in ophiolites at relatively shallow depths. However, the possibility for serpentinization to occur at greater depths, especially in subduction zones, raises new questions on the genesis of abiotic hydrocarbons at convergent margin and its impact on the deep carbon cycle. High-pressure ultramafic bodies exhumed in metamorphic belts can provide insights on the mechanisms of high-pressure serpentinization in subduction zones and on the chemistry of the resulting fluids. This study focuses on the ultramafic Belvidere Mountain complex belonging to the Appalachian belt of northern Vermont, USA. Microstructures show overgrowth of both primary (Mg# 0.91) and metamorphic (Mg# 0.95) olivine by delicate antigorite crystals, pointing to at least one stage of serpentinization at high-temperature conditions and consistent with the high-pressure subduction evolution of the Belvidere Mountain complex. Formation of ubiquitous magnetite and local Fe-Ni alloys testifies to the partial oxidation of Fe^{2+} into Fe^{3+} and generation of reduced conditions. Fluid inclusion trails cross-cutting the primary olivine relicts suggest their formation during the antigorite serpentinization event. MicroRaman spectroscopy on the fluid inclusions reveals a CH_4-rich gaseous composition, as well as N_2, NH_3 and H_2S. Moreover, the precipitation of daughter minerals such as lizardite and brucite in the fluid inclusions indicate the initial presence of H_2O in the fluid. High-pressure serpentinization driven by the infiltration of

metasediment-derived aqueous fluids is proposed at the origin of CH_4 and other reduced fluid species preserved in the fluid inclusions. This suggests the Belvidere Mountain complex as an example of deep abiotic hydrocarbon genesis related to high-pressure serpentinization in an early Paleozoic subduction zone.

Keywords: HP Serpentinization, Metamorphic olivine, Abiotic methane, C fluxes at subduction zones, Belvidere Mountain Complex.

Introduction

Alteration of ultramafic rocks by aqueous fluids, or serpentinization, produces serpentine-rich rocks and may be accompanied by redox reactions leading to the formation of H_2 and abiotic light hydrocarbons (Mével, 2003; Moody, 1976; Seyfried Jr et al., 2007). Oxidation of Fe^{2+} in mantle minerals and formation of Fe^{3+} minerals such as magnetite produces H_2, which may then promote the conversions of dissolved carbon-bearing species into abiotic CH_4 (Andreani et al., 2013; Berndt et al., 1996). Serpentinization is well documented at mid-ocean ridges and on land (Andréani et al., 2007; Cannat et al., 2010; Etiope et al., 2011; Klein et al., 2014; Schrenk et al., 2013), where H_2 and CH_4 produced through serpentinization can support biological communities and could be linked to the emergence of early life on Earth (Kelley et al., 2005; Ménez et al., 2018; Sleep and Bird, 2007). Serpentinization processes may also happen at much greater depths and affect subducted mantle sections and the overlying mantle wedge at convergent margins (Guillot et al., 2015, 2000; Vitale Brovarone et al., 2017; Wada et al., 2008), owing to the availability of aqueous fluids (Bebout and Penniston-Dorland, 2016; Deschamps et al., 2013). However, the patterns of serpentinization reactions at high-temperature (HT) and high-pressure (HP) conditions, here defined with respect to the serpentine stability field, and the associated fluid-rock redox budgets are still largely unconstrained. The possibility that HT-HP serpentinization may not involve Fe oxidation and genesis of H_2 has been proposed (Evans, 2010). However, natural case studies of slab-derived serpentinized peridotites suggest that magnetite, H_2 and abiotic CH_4 can be produced at these conditions (Vitale Brovarone et al., 2020). Ultramafic bodies in metamorphic belts can provide good insights on the mechanisms of HP-HT serpentinization and the resulting fluids (Evans et

al., 2017), and therefore make good case studies for the investigation of the mechanisms of serpentinization in subduction zones.

The Belvidere ultramafic complex, Vermont, USA, is a fragment of the Iapetus ocean that was involved in the Taconic orogeny and recorded HP metamorphism during Cambrian-Ordovician (Chew and van Staal, 2014; Gale, 1980; Honsberger et al., 2017). This complex includes variably serpentinized peridotites bearing antigorite, the HT serpentine polysome stable at subduction zone HP conditions (Schwartz et al., 2013), therefore making a potential example of HT-HP serpentinization. In this work, we integrate field, microstructural, thermodynamic, and fluid inclusions data to investigate the patterns and timing of serpentinization of the Belvidere ultramafic complex, with particular focus on the HP fluid-rock interactions recorded by these rocks.

1. Geologic setting

The Belvidere Mountain complex (BMC) area is part of a North-South trending belt of mafic/ultramafic rocks belonging to the Appalachian Mountain system and extending form Newfoundland to Georgia (Gale, 2007; Hibbard et al., 2006)(Fig. 1). These ultramafic bodies mainly consist of variably serpentinized peridotites, and associated metabasic and metafelsic rocks tectonically embedded within Cambrio-Ordovician metasedimentary and metavolcanics formations (Chidester et al., 1978; Gale, 1986, 1980; Laird et al., 1984; Van Baalen et al., 2009). The BMC, as well as other mafic/ultramafic complexes such as the Tillotson Peak and the Pennington complexes, are interpreted to represent remnants of an ocean-continent transition zone associated with the extension of the Laurentian margin (Chew and van Staal, 2014). These terranes were successively involved in the closure of the

Iapetus Ocean during the Ordovican Taconic orogeny (Doolan et al., 1982; Honsberger et al., 2017; Karabinos et al., 1998; Laird et al., 1984; Stanley et al., 1984). The BMC forms a 6.5 km long body that structurally overlies the metasedimentary Ottauquechee and Stowe Formations to the East and is overlain by the Hazen Notch formation to the West. The Stowe Formation is late Cambrian, composed of gray-green quartz -chlorite-sericite +/- magnetite schists. The Ottauquechee Formation is middle Cambrian consisting carbonaceous pyritiferous phyllite. The Hazen Notch Formation is dated from Neoproterozoic to Cambrian, graphitic and non-graphitic quartz-albite-sclerite-chlorite schist, along medium-grained, massive, quartz-albite-muscovite gneiss. The internal architecture of the BMC comprises, from top to bottom, variably serpentinized dunite and harzburgite, coarse-grained and fine-grained amphibolite, greenstone, muscovite schist, and albite gneiss (Gale, 1986, 1980; Van Baalen et al., 2009). Lenticular bodies composed of talc-carbonate rocks and steatite, often including cores of relatively unserpentinized peridotite, are observed within the BMC, and range size from a few meters to several tens of meter (Chidester et al., 1978). The BMC rocks underwent Taconic blueschist-facies peak metamorphic conditions constrained at 0.9-1.3 GPa and 510-520 °C in metabasic rocks (Honsberger, 2015; Laird et al., 1993). Slightly higher P, blueschist-to-eclogite-facies metamorphic conditions are recorded by the Tilliston Peak mafic rocks located just north of the BMC (Laird et al., 1993, 1984). This tectonometamorphic event has been dated at 505-473 Ma by $^{40/39}$Ar amphibole and mica geochronology (Castonguay et al., 2012; Laird et al., 1993).

2. Methods

Quantitative energy-dispersive X-ray spectroscopy (EDS) analyses and backscattered electron (BSE) imaging were carried out using the JSM-IT300LV Scanning Electron Microscope Oxford

Inca Energy Dispersive Spectrometer at the Department of Earth Sciences of Turin University. Data were processed with the INCA software from Oxford Instruments. Quantitative analysis employed 15kV accelerating voltage and 20 s to 40 s counting time. Natural and synthetic mineral and oxide standards were employed. EDS calibration was made using Cobalt standard.

Quantitative wavelength-dispersive spectrometer (WDS) analyses were carried out using a JEOL 8200 Super Probe at the Department of Earth Sciences "Ardito Desio" of Milan University. The microprobe was using a 15keV accelerating voltage under 5 nÅ, with 30s counting time under maximum emission peak. Sixteen oxide composition were measured, using synthetic and natural standards: grossular (Si, Al and Ca), omphacite (Na), K-feldspath (K), fayalite (Fe), forsterite (Mg), rhodonites (Mn), niccolite (Ni), ilmenite (Ti), galena (Pb and S), pure Cr, pure Zn and pure Cu.

MicroRaman spectroscopy of minerals and fluid inclusions was done at the Department of Earth Sciences, University of Turin, with a LabRAM HR (VIS) (HORIBA Jobin Yvon) equipped of a 532.11 nm, solid-state Nd laser, a Super Notch Plus filter with spectral resolution of 1 cm−1, and a grating of 600 grooves/mm. The laser of emission power was set at 80 mW and focused to 5 µm with a ×100 objective with a laser power on the sample < 5 mW. Calibration was performed using the 520.6 cm−1 band of a silicon standard for the 100-2000 cm^{-1} range, and the 2331 cm-1 band of atmospheric N_2 for the 2000-4000 cm^{-1} range. Four accumulations of 30–60 s were collected for each spectrum. Raman spectra of fluid inclusions were performed on double-polished thick sections unless otherwise specified.

89 Isotopic composition measurements of methane were performed on a MAT 253 (Thermo
90 Fisher) mass spectrometer, coupled with gas chromatography (GCC-IR-MS) in order to purify
91 the samples. The gas phase was extracted and measured after crushing the rock sampler
92 under vacuum.

93 Thermodynamic modelling was performed using the Deep Earth Water (DEW) Model
94 (Sverjensky et al., 2014) and the EQ3/EQ6 software (Wolery and Jarek, 2003) with a modified
95 Berman database (Berman, 1988). EQ3 was used to calculate the composition of a fluid in
96 equilibrium with a given mineral assemblage as, fO_2, P and T. EQ6 was used to model the
97 interaction of fluid compositions from EQ3 with another mineral assemblage as function of
98 the fluid/rock (F/R) ratio.

99 **3. Sample description and mineral chemistry**

100 In this section, we present the petrography, microstructures and mineral chemistry of
101 samples collected in the Belvidere mine (Fig. 2) and showing different degrees of
102 serpentinization. The selected samples range from weakly serpentinized dunite (V18-2a and
103 V18-2b) to partially serpentinized dunite including layers of boudinaged meta-pyroxenite
104 (V18-3a and V18-3b), to fully serpentinized peridotite (V18-B3).

105 **3.1. *Microstructural characterization***

106 Sample V18-2a (least serpentinized dunite) consists of olivine (~80 vol.%), antigorite (~10
107 vol.%), Cr-spinel (>5 vol.%), magnetite (<5 vol.%), chlorite (<1 vol.%), sulphides (<1 vol.%), and
108 alloys (<1 vol.%) determined from visual estimate in thin section. Primary olivine forms
109 crystals ranging in size from 0.25 to 1 mm (Fig. 3A). It is partially replaced by antigorite, as

identified by MicroRaman spectroscopy (Fig. 4), along mesh-like structures (Fig. 3A-C). Antigorite is present as elongated crystals, up to 200 μm in length, which statistically overgrew the olivine (Fig. 3C). Magnetite is present in three microstructural domains: as large, millimeter scale crystals rimming chromite relicts, as grains of ~50 μm in the mesh structures, and as millimeter scale crystals in antigorite veins. Chlorite is found, together with magnetite, around Cr-spinel relicts (Fig. 3B).

Sample V18-2b (serpentinized dunite) consists of antigorite (~40 vol.%), olivine (~40 vol.%, including primary and metamorphic olivine), magnetite (>5 vol.%), chlorite (>5 vol.%), brucite (<5 vol.%), and alloys (<1 vol.%). The structure is similar to V18-2a, but in this case the extent of serpentinization along the meshes is higher. SEM backscattered-electron imaging reveals the presence of a second generation of olivine, hereafter metamorphic olivine (see Section 4.2 for discussion) growing in two different sites: epitaxially on the primary olivine and replacing former orthopyroxene (Fig. 5A-B). Striped zoning is observed in primary olivine (Fig 5A), as described in Plümper et al., 2012a, alternating thin forsterite-richer and forsterite-poorer olivine composition. The initial presence of orthopyroxene in the rock is inferred based on the presence of clinopyroxene exsolutions preserved in metamorphic olivine-rich pseudomorphoses (Fig. 3D and 5B). Antigorite is present as elongated (0.5 mm in length) crystals and as fine-grained aggregates in the matrix. The elongated antigorite crystals are chemically zoned, with bright core and dark rim in backscattered electron imaging (Fig. 5A). Raman spectra of both generations exhibit the characteristic 1043 cm^{-1} band of antigorite, whereas the main OH stretching is at 3664 cm^{-1} in the bright core and at 3673 cm^{-1} in the dark rim (Fig 4C), both inconsistent with antigorite-lizardite mixing. The higher Raman shift of the dark rim may be linked to variation of pressure condition (Auzende et al., 2004). The dark

antigorite generation appears the same forming the fine-grained aggregates. The bright antigorite generation (at the core of large crystals) is never found in contact with either primary or metamorphic olivine, whereas the darker antigorite generation (at the rim of large crystals of disseminated in the matrix) is in contact with them (Fig. 5A). Magnetite is more abundant relative to sample V18-2a, especially along meshes. Brucite was identified by SEM and Raman (Fig. 4D) in veins, sometimes associated with metamorphic olivine (Fig. 5C). Alloys and sulphides are present in association with antigorite and are locally associated to magnetite (Fig. 5D).

Samples V18-3a and 3b are from a boudinaged layer of clinopyroxenite included in an intensely serpentinized dunite (Fig. 3E-G). The mineral assemblage and microstructures of the serpentinized dunite part of the sample is similar to sample V18-2b, yet more intensely serpentinized. The primary clinopyroxene is fully replaced by diopside aggregates in both the clinopyroxenite layer and the host dunite. The primary clinopyroxene sites in this sample are slightly different from the serpentinized dunite, with less abundant magnetite and characteristic fan-shaped diopside aggregates in the former compared to the latter. Metamorphic olivine is present at the rim of primary clinopyroxene and along its cleavages, together with antigorite (Fig. 5E-F). In the latter case, metamorphic olivine is localized along thin arrays encircled by antigorite (Fig. 5F). Antigorite shows the same chemical zoning as observed in the dunite, with brighter cores and darker rims in backscatter electron imaging (Fig. 5G). Backscattered electron imaging reveals that the dark antigorite shows similar overgrowth microstructural relationships with both primary and metamorphic olivine (Fig. 5E). The microstructures reflect either equilibrium between antigorite and the two olivine generations, or overgrowth of both olivine generations by the antigorite. Considering that the

amount of primary olivine strongly decreases in favour of antigorite in several samples, which suggests serpentinization of the primary olivine, second antigorite generation formed after the growth of metamorphic olivine appears . It is possible, even though the microstructures could not confirm it, that the first antigorite generation grew prior to or together with the metamorphic olivine. Magnetite is present in four different structural sites: as arrays of ~50 µm size crystals along the meshes, as trails of ~50 µm crystals in primary olivine and clinopyroxene pseudomorphoses, as aggregates rimming the primary Cr-spinel, and as millimeter scale aggregates along discordant veins. The Cr-spinel sites are characterized by three different layers: a rather preserved core, a mantle of ferritchromite, and a rim of magnetite (Fig. 5E; see Section 4.2).

Sample V18-B3 is a fully serpentinized peridotite. The matrix is composed of a mixture of antigorite and chrysotile (identified by MicroRaman) with magnetite. Brucite is observed replacing pyroxene sites and is associated with magnetite and/or metamorphic olivine (Fig. 3H and 5H). Based on the microstructural observations on sample V18-2b, these pseudomorphoses are interpreted as former orthopyroxene crystals replaced by metamorphic olivine and successively hydrated to form serpentine + brucite ± magnetite.

3.2. Mineral chemistry

Primary olivine has Mg# of 0.91-0.92 [Mg# = Mg/(Fe+Mg)], whereas metamorphic olivine is enriched in Mg (Mg# of 0.95) (Table 1, Fig. 6). The Mn# [Mn# = Mn/(Mn+Fe+Mn+Ni)] of metamorphic olivine (0.0040 ±0.0006) is much higher than primary olivine (0.0015 ±0.0005). Metamorphic olivine analyses in sample V18-B3 show slightly lower Mg# and higher Mn# content relative to metamorphic olivine from other samples. Metamorphic olivine rimming

178 the primary orthopyroxene sites in sample V18-3a has higher CaO content (0.25 wt.%)
179 compared to the metamorphic olivine overgrowing primary olivine in V18-2b (0.02 wt.%).
180 Metamorphic olivine in the sample V18-B3 show slightly lower Mg# and highly increased MnO
181 content (1.2 wt %) in regard to metamorphic olivine from other samples. The NiO content of
182 primary olivine (0.38 to 0.49 wt.%) and metamorphic olivine (0.39 to 0.46 wt.%) are similar.

183 The incorporation of Mn in olivine appears to be characteristic of metamorphic olivine from
184 several localities regardless of the olivine formation environments (dehydration vs.
185 hydration). The Mg# of metamorphic olivine relative to primary olivine may depend upon
186 several parameters such as the stability of different Fe-bearing minerals, the Fe partitioning
187 among them, and the P-T and redox conditions (Frost and Beard, 2007; Majumdar et al., 2016;
188 Nozaka, 2018, 2003). An increase in Mg# (and MnO) in metamorphic olivine relative to
189 primary olivine has been observed in inferred mantle wedge peridotites recording HP
190 serpentinization (Dandar et al., 2019; Guillot et al., 2000). Plümper et al., 2012a report striped
191 Mg# zoning in hydrated supra-subduction mantle rocks as the result of chemical interaction
192 during antigorite serpentinization at high temperature conditions. Metamorphic olivine
193 formed through prograde antigorite + brucite dehydration shows either lower or higher Mg#
194 compared to mantle olivine (Arai et al., 2012; Debret et al., 2013; Iyer et al., 2008; Kempf and
195 Hermann, 2018; Nozaka, 2018; Plümper et al., 2012b; Scambelluri et al., 1995; Shen et al.,
196 2015)(Fig. 6).

197 The core of individual, elongated antigorite crystals exhibits higher FeO (1.6 to 2.6 wt.% [Mg#
198 0.94-0.96]), Al_2O_3 (1.77 wt.%) [Mg# =Mg/(Mg+ΣFe)], and Cr_2O_3 (0.61 wt.%) than the rim (1.35
199 wt.% [Mg# 0.97], 0.52 wt.%, 0.13 wt.%, respectively) (Table 1). Unzoned matrix antigorite has

200 a composition equivalent to the rim of the elongated antigorite crystals. The Mn# [Mn# =
201 Mn/(Mn+Fe+Mn+Ni)] of antigorite is 0.0006 (±0.0004).

202 The preserved spinel core has Cr# [Cr/(Cr+Al)] of 0.79 (Table 2). The mantle overgrowing the
203 primary spinel has a ferritchromite mantle of Cr-magnetite with a Cr# of 0.91 and higher MnO
204 relative to the core. The magnetite rims with no Al_2O_3, but high Cr_2O_3 (1.87 wt.%). The
205 composition of magnetite in the meshes and veins differs from magnetite found in the spinel
206 sites, with very little Cr_2O_3.

207 Diopside has a Mg number [Mg# =Mg/(Mg+Fe)] of 0.98. Chlorite has an Mg# [Mg#
208 =Mg/(Mg+ΣFe)] of 0.95, and Cr_2O_3 up to 4.07 wt.% (Table 1).

209 Brucite has up to 3 wt.% FeO (as total Fe), Mg# [Mg# =Mg/(Mg+Fe)] of 0.97 (Table 2). Alloys
210 and sulfides are Ni rich, with various amounts of S, Fe and trace amounts of Pb, Cu, et Co
211 (Table 3). Alloys mainly consist of Cu-bearing FeNi alloy (taenite) (Table 3). Sulphides include
212 Ni, Cu, and Fe sulphides. Only heazlewoodite (NiS) was analysed whereas for other sulphides
213 proper analyses could not be obtain owing to the small grain sizes.

214 **3.3. Fluid inclusion analysis**

215 Primary olivine in all samples is rich in fluid inclusions forming secondary trails (Fig. 7). The
216 fluid inclusion trails are confined within individual crystals and show two alternative structural
217 relationships relative to the antigorite veins, being either cut by them (Fig. 7A) or injected
218 from them (Fig. 7B-C). These patterns suggest a secondary fluid trapping during the antigorite
219 serpentinization event forming the main mesh structure observed in the rock.

Fluid inclusions exhibit rounded to elongated shapes (Fig. 7D-E). Optical microscope observations at room conditions suggest that the fluid inclusions are either single-phase and gaseous, or bi-phase with solid and gas. MicroRaman spectra of fluid inclusions are presented in Fig. 8. The spectra show the presence of marked CH_4 bands (2912 cm^{-1}), as well as N_2 (2327 cm^{-1}), NH_3 (3324 cm^{-1}), S-H/H_2S (2575 cm^{-1}). Free H_2O in the fluid inclusions was not detected by MicroRaman. However, the presence of tiny amounts of free H_2O in the fluid inclusions — undetectable by MicroRaman at room conditions— cannot be excluded (Berkesi et al., 2009; Lamadrid et al., 2017).

The molar fraction of gas in the gas mixture was estimated using the Raman scattering cross-section and the instrumental efficiency of each species. Using equation presented in Frezzotti *et al.*, 2012, we obtain the following molar proportion: CH_4 = 92±6%, N_2 = 6±5%, H_2S = 1±1% and NH_3 = 1±2% for the mean composition of twenty inclusions in olivine from all samples (Fig 9). Composition within the same inclusion trail show molar fractionation variation smaller than 1% but different trail within the same crystal can exhibit up to 10% of molar fraction of CH_4 and could reflect fluid heterogeneity. Alternatively, this effect can be the result of different crystal orientation during data acquisition (Caumon et al., 2019). No clear pattern was observed linked to relationship between inclusion trails and antigorite veinlets.

Solid phases were identified in large fluid inclusions. MicroRaman analysis revealed the presence of lizardite and brucite but no magnetite was detected. Some inclusions contain graphite as a solid phase in the inclusion in addition (Fig. 7F and Fig. 8B). The only sporadic presence of graphite in the fluid inclusions, and in particular in inclusions resulting from necking processes, suggest that this mineral precipitated as a result of local respeciation of the fluid inclusions (Cesare, 1995). The presence of hydrous phases is the inclusions suggests

243 re-equilibration of the inclusion with the host mineral, effectively serpentinizing the olivine
244 and consuming water initially present in the inclusions. However, the presence of step-
245 daughter minerals in the inclusion is not systematic, suggesting that the initial fluid was
246 already rich in CH_4 (-N_2-NH_3-H_2S) at the time of trapping, and that the reduced fluid species
247 did not form only inside the fluid inclusions.

248 **3.4. Rodingite**

249 Rodingite are ultramafic rocks that are composed of carbonate, garnet, diopside, epidote ±
250 graphite. While not being the focus of this study, the carbonate in the rodingite bear
251 numerous trails of fluid inclusions. Fluid inclusions exhibit negative crystal shape and are
252 single-phase gaseous. The composition of the carbonate-hosted fluid inclusions, as revealed
253 by Raman spectroscopy, is essentially CH_4 and N_2. Using quantitative estimation of inclusions
254 in carbonates (see section 4.3) yield molar fractions of N_2 = 67±4%, CH_4 = 33±4% on four
255 different inclusions.

256 **3.5. Thermodynamic modelling**

257 Thermodynamic calculations were performed in order to constrain the mineralogical, fluid
258 and redox pattern of the HP serpentinization. Because the selected partially serpentinized
259 samples are comprised in strongly serpentinized rocks and embedded in metasediment, two
260 fluid equilibriums can be considered. For silica-rich fluid sources (e.g. metasedimentary rocks
261 or talc-bearing ultramafic rocks), the predicted assemblages do not match the natural
262 samples. For this reason, the fluid composition calculated with EQ3 was equilibrated with a
263 serpentinite consisting of antigorite + magnetite + brucite + chlorite + olivine. This fluid then
264 reacted with a dunite with mineral modal proportions comparable with the study samples

and consisting of 92% olivine (forsterite 90%, fayalite 10%), 5.4% orthopyroxene (enstatite 90%, ferrosilite 10%), 2.5% clinopyroxene (diopside 90%, hedenbergite 10%) and 0.1% spinel. The fO_2 of the infiltrating fluid was set at the quartz-fayalite-magnetite (QFM) buffer. The calculations were done at temperatures consistent with the peak metamorphic conditions estimated for the BMC, i.e., 400 °C to 500 °C and 1 GPa (Honsberger, 2015; Laird et al., 1993), and for different F/R ratios. Figure 10 shows the mineralogical evolution as a function of reaction progress at 450 °C and 1GPa for a fluid rock ratio of 1. The model reaction proceeds with progressive transformation of, from the first to the last reacting mineral, mantle spinel, clinopyroxene, orthopyroxene, and olivine. Magnetite starts to form during the early stages of the reaction along with chlorite in response to spinel consumption. Reaction of mantle pyroxenes marks the precipitation of metamorphic clinopyroxene (diopside 93%, hedenbergite 3.35% and clino-enstatite 3.65%), metamorphic olivine, antigorite, and additional magnetite. The late formation of antigorite marks the partial consumption of metamorphic olivine and a decrease in its Mg#, from Mg# 0.90 to Mg# 0.83. These patterns reflect the microstructural features observed in the natural samples. For example, spinel appears intensely replaced by chlorite in rather unserpentinized portions of the rock (Fig. 10A). Similarly, mantle olivine adjacent to fully replaced mantle pyroxenes is commonly little affected by the serpentinization. Both mantle and metamorphic olivine in the natural samples appear texturally replaced by antigorite, as also suggested by the modelling while approaching equilibration. With the chosen bulk composition and used thermodynamic data set, the formation of antigorite is limited to T < 470 °C. The antigorite stability field could be enlarged by considering iron in the antigorite thermodynamic model. The fO_2 decreases progressively during the reaction progress, with a steep decrease during the formation of antigorite down to ΔLog QFM = -1.2 (Fig. 10C). Methane, initially about 1 order of magnitude

289 less concentrated than CO_2 in the reacting fluid, becomes a dominant species at reaction
290 completion (about 1 order of magnitude more concentrated than CO_2). Nevertheless,
291 variations of parameters such as F/R ratio, mineralogy, or temperature, were found to affect
292 the proportion of CH_4 and CO_2. As an example, increasing the modal proportion of either
293 orthopyroxene or clinopyroxene in the initial rock or decreasing the F/R ratio appears to
294 favour a higher proportion of CH_4 in the fluid in respect to CO_2. The model predicts high
295 relative concentration of H_2 in the fluids, however H_2 was not detected in natural samples by
296 micro-Raman spectroscopy. Sulphur and nitrogen speciation were also assessed, with HS^- and
297 H_2S and NH_3 being the dominant sulphur species relative to HSO_4^- and N_2 and NH_4^+,
298 respectively (Fig. 10B).

299 **4. Discussion**

300 **4.1. Patterns and timing of serpentinization**

301 The timing of serpentinization of slab-derived, exhumed HP serpentinized rocks can span
302 (sub)seafloor conditions prior to subduction, prograde hydration during subduction, or
303 retrograde hydration during exhumation. The BMC complex has been interpreted as a
304 fragment of subducted Iapetus lithosphere, and therefore may have recorded different stages
305 of serpentinization. Although the possibility of at least some (sub)seafloor serpentinization
306 prior to the Taconic subduction cannot be excluded, our data cannot provide any proof of
307 such a pre-subduction event and, instead, suggest a main hydration event at HP-HT conditions
308 in the subduction zone.

309 Besides late chrysotile veinlets, antigorite is the only serpentine polysome identified in the
310 BMC rocks. Although formation of antigorite may occur in a wide range or P-T conditions also
311 as a function of chemical parameters such as the silica activity (Rouméjon et al., 2019),

312 serpentinites dominated by antigorite are generally referred to the HT temperature part of
313 the serpentine stability field, generally above ~300-400 °C (Evans, 2004; Schwartz et al.,
314 2013). In most subduction zone settings, these conditions also correspond to relatively HP
315 conditions above 1 GPa. However, the presence of antigorite does not necessarily imply the
316 serpentinization event to have happened at HP-HT conditions because it could also have
317 formed as a result of the prograde transformation of lizardite or chrysotile following the
318 reaction:

319 17 Lizardite/Chrysotile = Antigorite + 3 Brucite (1)

320 Nevertheless, several lines of evidence indicate that the BMC rocks recorded a stage of HP-
321 HT serpentinization. As a first general consideration, the presence of fresh mantle
322 assemblages throughout the complex (Chidester *et al.*, 1978; this study) represents a suitable
323 condition to promote HP-HT serpentinization in the subduction zone, if aqueous fluids are
324 available. Such a process has already been proposed in other HP ultramafic massifs preserving
325 fresh mantle assemblages (e.g. Früh-Green et al., 2004; Scambelluri and Tonarini, 2012; Vitale
326 Brovarone et al., 2020, 2017). The BMC rocks provides evidence for such a HP hydration event.
327 Figure 11 summarizes the proposed fluid-rock evolution of the BMC rocks as inferred from
328 the studied samples. The first indication of serpentinization (stage I in Fig. 11) is suggested by
329 the growth of elongated metamorphic olivine on the primary clinopyroxene sites (Fig. 5G),
330 which suggests the former presence of serpentine blades overgrowing the primary
331 clinopyroxene. The selective growth of serpentine at the expense of clinopyroxene rather
332 than primary olivine places this hypothetical event at HT conditions (Klein et al., 2013) and
333 possibly in the antigorite stability field (Fig. 12). Metamorphic olivine is most commonly
334 interpreted to form in response of serpentine dehydration during prograde metamorphism

(Plümper et al., 2017; Scambelluri et al., 1991). Figure 12 provides a compilation of traditional serpentine dehydration reactions leading to the formation of metamorphic olivine. The peak metamorphic conditions proposed for the BMC (0.9-1.3 GPa and 520 °C) are consistent with the first olivine-forming reaction involving antigorite + brucite as reactants. Moreover, several studies have shown that olivine can form at T conditions lower than the reactions shown in figure 12 as a result of local bulk compositional features (Plümper et al., 2017). Alternatively, metamorphic olivine after orthopyroxene may also have formed in response to hydration rather than dehydration reactions, as already proposed for serpentinized mantle wedge rocks (Dandar et al., 2019) following the reaction:

Orthopyroxene + 0.46 Water + 0.35 Mg^{2+}=

0.59 M-olivine +0.06 Antigorite + 0.29 Silica + 0.7 H^{+} (2)

Followed by the hydration of olivine to form antigorite following the reaction

Olivine + 1.29 Water + 0.42 Silica = 0.71 Antigorite (3)

In either case (hydration or dehydration), the amount of serpentinization predating the formation of metamorphic olivine must have been very low and, if any, related to a HT event.

The second, more robustly constrained stage of transformation (stage II in Fig. 11) is characterized by the formation of metamorphic olivine after primary orthopyroxene, and as rim around primary clinopyroxene (now recrystallized into diopside). This reaction was observed in rocks containing rather undisturbed primary olivine, which again point to HT serpentinization conditions (Klein et al., 2013). The partial preservation of clinopyroxene exsolution lamellae inside metamorphic olivine pseudomorphic on orthopyroxene may suggest nearly isovolumetric replacement during this event (Plümper et al., 2012b; Viti et al.,

2005). The thermodynamic modeling results suggest that, at 450 °C and 1 GPa, a transient antigorite generation may have formed together with metamorphic olivine early in the fluid-rock interaction, along with spinel breakdown. The Al-Cr-rich antigorite cores (Atg1) observed in the studied samples may testify to this transient antigorite formation. The application of empirical distribution coefficient K_D for antigorite and olivine by Evans, 2008 and Trommsdorff and Evans, 1974 support this hypothesis (Table 4). The empirical Mg distribution coefficient K_D [antigorite/olivine, $K_D = (\sum Fe/Mg_{Srp})/(Fe/Mg_{Ol})$] proposed by Evans, 2008 is 0.45-0.35 upon consideration of ferric iron in the antigorite. The Atg1/metamorphic olivine apparent K_D is 0.49-0.25, which agrees with the value proposed by Evans, 2008 for equilibrium, compared with other antigorite/olivine pairs (Atg1/primary olivine = 0.14-0.25; matrix antigorite (Atg2)/primary olivine = 0.11; Atg2/metamorphic olivine = 0.17-0.25). The Mn distribution between antigorite and olivine gives similar results. The empirical Mn distribution coefficients for antigorite/olivine equilibria is 0.18 (Trommsdorff and Evans, 1974). The Atg1/metamorphic olivine pair has apparent appears K_D of 0.14-0.18, thus consistent with the predicted equilibrium (Table 4).

The third stage (stage III in Fig. 11) is characterized by the growth of a matrix antigorite (Atg2) at the expense of both primary and metamorphic olivine. This event may mark either retrograde hydration along the exhumation path of the BMC, or the progression of the fluid-rock interaction. As indicated by the thermodynamic modeling results, a second antigorite generation is expected to form at 450 °C and 1 GPa after the precipitation of metamorphic olivine (Fig. 10A). The modeling predicts this second antigorite and metamorphic olivine to be stable together. However, the apparent K_D for matrix antigorite and metamorphic olivine suggest disequilibrium (equilibrium Mg K_D = 0.45, measured = 0.17-0.25; equilibrium Mn K_D =

380 0.18, measured = 0.09-0.14) (Table 4). This feature suggests that stage III marks the beginning
381 of retrograde hydration.

382 The fourth stage of serpentinization (IV in Fig. 11) is characterized by the complete
383 serpentinization of primary olivine and partial to full serpentinization of metamorphic olivine.
384 The partial preservation of metamorphic olivine after orthopyroxene in sample free of any
385 primary olivine relict indicates that the largest event of serpentinization of the BMC rocks
386 took place after the formation of metamorphic olivine. The presence of both antigorite and
387 lizardite + brucite at the expense of metamorphic olivine after orthopyroxene suggests that
388 this event protracted during the cooling of the BMC metamorphic path to temperatures lower
389 than 400 °C (Fig. 12).

390 In summary, based on the collected petrographic and thermodynamic data, the dominant
391 serpentinization event observed in the BMC complex is interpreted to have taken place in the
392 Taconic subduction zone.

393

394 **4.2. Timing of fluid inclusion formation and origin of CH_4**

395 **4.2.1. Timing of fluid inclusion entrapment**

396 Fluid inclusions in the BMC ultramafic and related metasomatic rocks contain reduced fluid
397 species such as CH_4, NH_3, and H_2S. The timing of fluid inclusion formation, as well as the origin
398 of their reduced speciation, is discussed in this section.

399 Reduced fluids have been found to form in ultramafic systems in a wide range of geologic
400 conditions spanning mid-ocean ridges, obducted ophiolitic massifs, and orogenic peridotite
401 bodies, in subduction, and in the upper mantle (Andréani et al., 2007; Etiope et al., 2011;

Schrenk et al., 2013). In the BMC rocks, the fluid inclusions may have formed in three different stages of the evolution of the massif and corresponding to three different geodynamic settings: (i) in the mantle prior to the formation of the Iapetus Ocean, (ii) during the (sub)seafloor evolution prior to subduction, and (iii) in the subduction zone.

A primary mantle origin can be ruled out because the observed fluid inclusions occur as secondary trails propagating from the antigorite veinlets crossing olivine crystal. A (sub)seafloor origin would match the identification of CH_4-rich fluid inclusions in oceanic peridotite (Cannat et al., 2010; Holm and Charlou, 2001). However, in this case, the fluid inclusions would have been preserved during prograde metamorphism to at least 520 °C and 1 GPa, which is unlikely (Touret, 2001). Moreover, the BMC fluid inclusions are rich in N species (NH_3, N_2), which seems to be an uncommon feature in fluid inclusions from oceanic peridotites (Grozeva et al., 2020; Klein et al., 2019). Instead, N-rich, NH_3-bearing fluid inclusions have been recently documented in CH_4-rich fluid inclusions in HP serpentinized peridotites from the Alpine belt and proposed to represent a distinctive feature of subduction zone serpentinizing fluids relative to mantle or (sub)seafloor fluids, especially in the presence of metasediment-derived fluids (Vitale Brovarone et al., 2020). Considering the microstructural and petrologic features discussed in Section 5.1, and the abundance of N species, a metamorphic origin in the Taconic subduction is proposed for the studied fluid inclusions.

The formation of lizardite and brucite as step-daughter minerals inside the fluid inclusions can be interpreted (1) as a prograde, pre-antigorite inclusion-host interactions, (2) as a retrograde reequilibration of antigorite during cooling of the BMC below ~400 °C with excess brucite (Reaction 1), or (3) as a retrograde host-inclusion interaction below ~400 °C (Fig. 12).

Excluding lizardite (meta)stability due to local equilibrium/kinetic features or faster antigorite-lizardite conversion in the inclusions relative to the host rock, we interpret the formation of step-daughter lizardite and brucite as a retrograde host-inclusion interaction. Similar interpretations have been proposed for analogous inclusions from Alpine belt (Vitale Brovarone et al., 2020).

4.2.2. Origin of the reducing potential and fluid sources

Another important question is the origin the identified reduced fluids species. In particular, several studies over the last decades have investigated the biotic or abiotic origin of geological CH_4 and associated reduced fluid species (Etiope et al., 2011; Etiope and Sherwood Lollar, 2013; McCollom, 2016; Ménez et al., 2018). Ultramafic systems are generally favourable environments for the genesis of abiotic CH_4 (Section 5.2.1), but other interpretations are also possible.

For example, the abundance of metasedimentary rocks in the study area may have promoted the formation of thermogenic gases during their prograde evolution. This hypothesis would be also consistent with the production of NH_3 through degassing of organic matter in metasedimentary rocks (Bebout and Fogel, 1992; Li et al., 2009). Biotic processes, including thermogenic gas formation, typically show very light $\delta^{13}C_{CH4}$ signatures (Etiope and Sherwood Lollar, 2013), whereas abiotic processes generally result in much heavier $\delta^{13}C_{CH4}$ (~-50 to 0‰) (Etiope and Sherwood Lollar, 2013). In order to test this hypothesis, we performed reconnaissance $\delta^{13}C$ analysis of CH_4 in the fluid inclusions (Boutier et al., in preparation). The analyses yielded $\delta^{13}C$ in the range of -14‰ (±2‰) for inclusions in olivine, and -13‰ (±1‰) for carbonate-hosted methane-rich inclusions from the rodingite. Even though these results

must be considered as preliminary test data, they seem to exclude the possibility of a pure thermogenic source.

Following the hypothesis of an abiotic origin, two possible mechanisms for the formation of CH_4 can be considered with either external or internal sources, respectively. External sources correspond to the infiltration of CH_4 and other reduced species formed abiotically in other geological reservoirs. A deep mantle origin for the reduced fluids detected in the BMC fluid inclusions appears unlikely if the syn-inclusion, water-rich nature of the serpentinizing fluid is considered. The metasedimentary formations adjacent to the BMC contain carbonate, graphitic carbon, sulphides, and phyllosilicates as potential sources of the C-N-S-H fluid identified in the fluid inclusions. Previous studies along the Appalachian belt have reported evidence of carbon mobilization from these metasedimentary formations or their along-strike equivalents. For example, Zhang *et al.*, 2018 documented metamorphic loss of isotopically light carbon from the Wepawaug schists, Connecticut. The possibility for these carbonate-bearing formations to generate strongly reduced fluids abiotically is not obvious —for reference, water-maximum conditions in graphite-saturated fluids contain roughly equal proportions of CH_4 and CO_2 (Connolly, 1995; Holloway, 1984) —. Nevertheless, evidence for the circulation of CH_4-rich fluids in equivalent formations in East Central Vermont and New Hampshire has been reported (Evans et al., 2002; Rumble III and Hoering, 1986). Nevertheless, most petrological studies focusing on New England metasediment-derived fluids point to more oxidized, CO_2-dominated aqueous fluids(Ferry, 2007; Penniston-Dorland and Ferry, 2006). Alternative external sources of reduced fluids would require unidentified processes, including mixing of different carbon reservoirs, or water-rock interactions equivalent to those that took place in the BMC.

A reducing potential internal to the BMC, and in particular the hydroxylation of fresh mantle peridotites during the Taconic subduction, appears the most likely interpretation for the genesis of the identified reduced fluid species. The presence of Fe-Ni alloys in the BMC partially serpentinized peridotites indicates that the rock recorded reducing conditions, as already observed in several oceanic and ophiolitic, and some subduction zone serpentinites (Evans et al., 2017; Frost, 1985; Klein and Bach, 2009; Vitale Brovarone et al., 2020). High-pressure syn-serpentinization reducing conditions are also suggested by the thermodynamic modelling results presented in this study, which indicates fO_2 values as low as –3.2 ΔQFM at 400 °C and 1 GPa to -1.2 ΔQFM at 450 °C and 1 GPa, and the formation of significant amounts of H_2 in the fluid (Fig. 10C). The interaction of this H_2 with dissolved carbon, nitrogen, and sulphur species present in the serpentinizing fluid, could have favoured the formation of CH_4 H_2S, and NH_3 from more oxidized species. For NH_3, the modelling also indicates that this species is already the dominant N species in the infiltrating fluid buffered at QFM. This feature suggests that the N_2 detected in the fluid is most likely formed through post-entrapment respeciation of NH_3, unless the serpentinizing fluid was more oxidized than QFM. The absence of detectable H_2O in the fluid inclusions is interpreted to result from host-inclusion interaction and formation of step-daughter lizardite and brucite, or by the preferential entrapment of immiscible reduced gases relative to aqueous fluids (Huang et al., 2017; Vitale Brovarone et al., 2017). The absence of residual H_2 in the fluid inclusions may be explained by the much faster diffusion H_2 relative to other fluid species through the host olivine, or by selective leakage.

The most plausible sources of serpentinizing fluid were the metasedimentary formations surrounding the BMC complex. These rock types host substantial amounts of subducted carbon, sulphur, and nitrogen (Bebout and Fogel, 1992; Evans et al., 2014; Kelemen and

Manning, 2015; Plank and Manning, 2019). An ultramafic source internal to the BMC would not be consistent with the general retention of N during prograde metamorphism and dehydration of serpentinites (Halama et al., 2014). The hypothesis of a metasediment-derived serpentinizing fluid was also suggested by previous oxygen and hydrogen isotopic data on antigorite from the BMC complex (Wenner and Taylor, 1974, 1971). Moreover, the authors proposed antigorite-magnetite equilibration T in the range of 220-460 °C, which is consistent with the prograde P-T of the BMC (Fig. 12). This supports the interpretation of a subduction-related serpentinization related to the infiltration of metasedimentary-derived fluids in a rather dry ultramafic body.

5. Conclusions

Mineralogical, microstructural, and fluid inclusion study of variably serpentinized dunite from the Belvidere Mountain Complex, Appalachian belt, Northern Vermont, provides insight into the process of high-pressure serpentinization in subduction zone and the related fluid-rock redox patterns. Although the BMC underwent a complex tectonic evolution potentially characterized by multiple stages of hydration from the (sub)seafloor to subduction and exhumation, the collected data point to a major event of high-pressure serpentinization that took place in the Appalachian subduction zone. Metamorphic olivine in the BMC serpentinized peridotite is interpreted as the product of rock hydration rather than dehydration, linked to the high-pressure serpentinization event. Our data support the hypothesis that the methane observed in olivine-hosted secondary fluid inclusions is genetically linked to serpentinization in the antigorite stability field consistent with the high-pressure portion of the prograde or retrograde P-T path of the BMC. This favors an abiotic origin for this methane, even though a biotic origin for the C source cannot be excluded. The

C- and N-rich composition of fluid inclusions suggests a metasediment-derived origin for the serpentinizing fluid. The high-pressure serpentinization and related abiotic methanogenesis place the Belvidere mountain complex as a suitable proxy for the study of mantle wedge serpentinization. This study confirms the importance of fluid mobility in deep seated ultramafic body in subduction zones for the mobility of C, H, and N, and their implications on large-scale geochemical cycling.

6. Acknowledgments

AVB acknowledges a MIUR Rita Levi Montalcini grant and a Richard Lounsbery Foundation grant. Simona Ferrrando is thanked for her helpful discussions and insights on fluid inclusions. IFP Energies Nouvelles and its helpful personnel is thanked for its help in the acquisition on test isotopic data of methane.

7. References

Andréani, M., Mével, C., Boullier, A.-M., Escartin, J., 2007. Dynamic control on serpentine crystallization in veins: Constraints on hydration processes in oceanic peridotites. Geochem. Geophys. Geosystems 8.

Andreani, M., Munoz, M., Marcaillou, C., Delacour, A., 2013. µXANES study of iron redox state in serpentine during oceanic serpentinization. Lithos 178, 70–83.

Arai, S., Ishimaru, S., Mizukami, T., 2012. Methane and propane micro-inclusions in olivine in titanoclinohumite-bearing dunites from the Sanbagawa high-P metamorphic belt, Japan: Hydrocarbon activity in a subduction zone and Ti mobility. Earth Planet. Sci. Lett. 353, 1–11.

Auzende, A.-L., Daniel, I., Reynard, B., Lemaire, C., Guyot, F., 2004. High-pressure behaviour of serpentine minerals: a Raman spectroscopic study. Phys. Chem. Miner. 31, 269–277.

Bebout, G.E., Fogel, M.L., 1992. Nitrogen-isotope compositions of metasedimentary rocks in the Catalina Schist, California: implications for metamorphic devolatilization history. Geochim. Cosmochim. Acta 56, 2839–2849.

Bebout, G.E., Penniston-Dorland, S.C., 2016. Fluid and mass transfer at subduction interfaces—The field metamorphic record. Lithos 240–243, 228–258. https://doi.org/10.1016/j.lithos.2015.10.007

Berkesi, M., Hidas, K., Guzmics, T., Dubessy, J., Bodnar, R.J., Szabó, C., Vajna, B., Tsunogae, T., 2009. Detection of small amounts of H2O in CO2-rich fluid inclusions using Raman spectroscopy. J. Raman Spectrosc. Int. J. Orig. Work Asp. Raman Spectrosc. High. Order Process. Also Brillouin Rayleigh Scatt. 40, 1461–1463.

Berman, R.G., 1988. Internally-consistent thermodynamic data for minerals in the system Na2O-K2O-CaO-MgO-FeO-Fe2O3-Al2O3-SiO2-TiO2-H2O-CO2. J. Petrol. 29, 445–522.

552 Berndt, M.E., Allen, D.E., Seyfried Jr, W.E., 1996. Reduction of CO2 during serpentinization of olivine
553 at 300 C and 500 bar. Geology 24, 351–354.
554 Cannat, M., Fontaine, F., Escartin, J., 2010. Serpentinization and associated hydrogen and methane
555 fluxes at slow spreading ridges. Divers. Hydrothermal Syst. Slow Spreading Ocean Ridges
556 188, 241–264.
557 Castonguay, S., Kim, J., Thompson, P.J., Gale, M.H., Joyce, N., Laird, J., Doolan, B.L., 2012. Timing of
558 tectonometamorphism across the Green Mountain anticlinorium, northern Vermont
559 Appalachians: 40Ar/39Ar data and correlations with southern Quebec. GSA Bull. 124, 352–
560 367. https://doi.org/10.1130/B30487.1
561 Caumon, M.-C., Tarantola, A., Wang, W., 2019. Raman spectra of gas mixtures in fluid inclusions:
562 Effect of quartz birefringence on composition measurement. J. Raman Spectrosc.
563 Cesare, B., 1995. Graphite precipitation in C—O—H fluid inclusions: closed system compositional and
564 density changes, and thermobarometric implications. Contrib. Mineral. Petrol. 122, 25–33.
565 Chew, D.M., van Staal, C.R., 2014. The ocean–continent transition zones along the Appalachian–
566 Caledonian Margin of Laurentia: Examples of large-scale hyperextension during the opening
567 of the Iapetus Ocean. Geosci. Can. 41, 165–185.
568 Chidester, A.H., Albee, A.L., Cady, W.M., 1978. Petrology, structure, and genesis of the asbestos-
569 bearing ultramafic rocks of the Belvidere Mountain area in Vermont. US Govt. Print. Off.,.
570 Connolly, J.A.D., 1995. Phase diagram methods for graphitic rocks and application to the system C-
571 O- H- FeO- TiO 2- SiO 2. Contrib. Mineral. Petrol. 119, 94–116.
572 Dandar, O., Okamoto, A., Uno, M., Oyanagi, R., Nagaya, T., Burenjargal, U., Miyamoto, T., Tsuchiya,
573 N., 2019. Formation of secondary olivine after orthopyroxene during hydration of mantle
574 wedge: evidence from the Khantaishir Ophiolite, western Mongolia. Contrib. Mineral. Petrol.
575 174, 86.
576 Debret, B., Nicollet, C., Andreani, M., Schwartz, S., Godard, M., 2013. Three steps of serpentinization
577 in an eclogitized oceanic serpentinization front (Lanzo Massif–Western Alps). J. Metamorph.
578 Geol. 31, 165–186.
579 Deschamps, F., Godard, M., Guillot, S., Hattori, K., 2013. Geochemistry of subduction zone
580 serpentinites: A review. Lithos 178, 96–127.
581 Doolan, B.L., Gale, M.H., Gale, P.N., Hoar, R.S., St-Julien, P., 1982. Geology of the Quebec re-entrant:
582 possible constraints from early rifts and the Vermont-Quebec serpentine belt. Major Struct.
583 Zones Faults North. Appalach. Ed. P St-Julien J Béland Geol. Assoc. Can. Spec. Pap. 24, 87–
584 115.
585 Etiope, G., Schoell, M., Hosgörmez, H., 2011. Abiotic methane flux from the Chimaera seep and
586 Tekirova ophiolites (Turkey): understanding gas exhalation from low temperature
587 serpentinization and implications for Mars. Earth Planet. Sci. Lett. 310, 96–104.
588 Etiope, G., Sherwood Lollar, B., 2013. Abiotic methane on Earth. Rev. Geophys. 51, 276–299.
589 Evans, B.W., 2010. Lizardite versus antigorite serpentinite: Magnetite, hydrogen, and life (?).
590 Geology 38, 879–882.
591 Evans, B.W., 2008. Control of the products of serpentinization by the Fe2+ Mg- 1 exchange potential
592 of olivine and orthopyroxene. J. Petrol. 49, 1873–1887.
593 Evans, B.W., 2004. The serpentinite multisystem revisited: chrysotile is metastable. Int. Geol. Rev.
594 46, 479–506.
595 Evans, K.A., Bickle, M.J., Skelton, A.D.L., Hall, M., Chapman, H., 2002. Reductive deposition of
596 graphite at lithological margins in East Central Vermont: a Sr, C and O isotope study. J.
597 Metamorph. Geol. 20, 781–798.
598 Evans, K.A., Reddy, S.M., Tomkins, A.G., Crossley, R.J., Frost, B.R., 2017. Effects of geodynamic
599 setting on the redox state of fluids released by subducted mantle lithosphere. Lithos 278–
600 281, 26–42. https://doi.org/10.1016/j.lithos.2016.12.023
601 Evans, K.A., Tomkins, A.G., Cliff, J., Fiorentini, M.L., 2014. Insights into subduction zone sulfur
602 recycling from isotopic analysis of eclogite-hosted sulfides. Chem. Geol. 365, 1–19.

603 Ferry, J.M., 2007. The role of volatile transport by diffusion and dispersion in driving biotite-forming
604 reactions during regional metamorphism of the Gile Mountain Formation, Vermont. Am.
605 Mineral. 92, 1288–1302.
606 Frezzotti, M.L., Tecce, F., Casagli, A., 2012. Raman spectroscopy for fluid inclusion analysis. J.
607 Geochem. Explor. 112, 1–20.
608 Frost, B.R., 1985. On the stability of sulfides, oxides, and native metals in serpentinite. J. Petrol. 26,
609 31–63.
610 Frost, B.R., Beard, J.S., 2007. On silica activity and serpentinization. J. Petrol. 48, 1351–1368.
611 Früh-Green, G.L., Connolly, J.A., Plas, A., Kelley, D.S., Grobéty, B., 2004. Serpentinization of oceanic
612 peridotites: implications for geochemical cycles and biological activity. Subseafloor
613 Biosphere -Ocean Ridges 144, 119–136.
614 Gale, M.H., 2007. Bedrock Geologic Map of the Hazens Notch and Portions of the Eden and Lowell
615 Quadrangles, Vermont. Vt. Geol. Surv., Vermont geological open file report VG07-2, plate 1.
616 Gale, M.H., 1986. Geologic map of the Belvidere Mountain area, Eden and Lowell, Vermont (USGS
617 Numbered Series No. 1560), IMAP.
618 Gale, M.H., 1980. Geology of the Belvidere Mountain Complex, Eden and Lowell, Vermont. US
619 Geological Survey,.
620 Grozeva, N.G., Klein, F., Seewald, J.S., Sylva, S.P., 2020. Chemical and isotopic analyses of
621 hydrocarbon-bearing fluid inclusions in olivine-rich rocks. Philos. Trans. R. Soc. A 378,
622 20180431.
623 Guillot, S., Hattori, K.H., de Sigoyer, J., 2000. Mantle wedge serpentinization and exhumation of
624 eclogites: insights from eastern Ladakh, northwest Himalaya. Geology 28, 199–202.
625 Guillot, S., Schwartz, S., Reynard, B., Agard, P., Prigent, C., 2015. Tectonic significance of
626 serpentinites. Tectonophysics 646, 1–19.
627 Halama, R., Bebout, G.E., John, T., Scambelluri, M., 2014. Nitrogen recycling in subducted mantle
628 rocks and implications for the global nitrogen cycle. Int. J. Earth Sci. 103, 2081–2099.
629 Hibbard, J.P., Van Staal, C.R., Rankin, D.W., Williams, H., 2006. Lithotectonic map of the Appalachian
630 orogen, Canada–United States of America. Geol. Surv. Can. Map A 2096, 2.
631 Holloway, J.R., 1984. Graphite-CH4-H2O-CO2 equilibria at low-grade metamorphic conditions.
632 Geology 12, 455–458.
633 Holm, N.G., Charlou, J.L., 2001. Initial indications of abiotic formation of hydrocarbons in the
634 Rainbow ultramafic hydrothermal system, Mid-Atlantic Ridge. Earth Planet. Sci. Lett. 191, 1–
635 8.
636 Honsberger, I.W., 2015. Metamorphism, deformation, geochemistry, and tectonics of exhumed
637 ultramafic and mafic rocks in the central and north-central Vermont Appalachians.
638 Honsberger, I.W., Laird, J., Thompson, P.J., 2017. A tectonized ultramafic-mafic-pelitic package in
639 Stockbridge, Vermont: Metamorphism resulting from subduction and exhumation. Am. J.
640 Sci. 317, 1019–1047.
641 Huang, F., Daniel, I., Cardon, H., Montagnac, G., Sverjensky, D.A., 2017. Immiscible hydrocarbon
642 fluids in the deep carbon cycle. Nat. Commun. 8, 1–8.
643 Iyer, K., Austrheim, H., John, T., Jamtveit, B., 2008. Serpentinization of the oceanic lithosphere and
644 some geochemical consequences: constraints from the Leka Ophiolite Complex, Norway.
645 Chem. Geol. 249, 66–90.
646 Karabinos, P., Samson, S.D., Hepburn, J.C., Stoll, H.M., 1998. Taconian orogeny in the New England
647 Appalachians: Collision between Laurentia and the Shelburne Falls arc. Geology 26, 215–218.
648 https://doi.org/10.1130/0091-7613(1998)026<0215:TOITNE>2.3.CO;2
649 Kelemen, P.B., Manning, C.E., 2015. Reevaluating carbon fluxes in subduction zones, what goes
650 down, mostly comes up. Proc. Natl. Acad. Sci. 112, E3997–E4006.
651 https://doi.org/10.1073/pnas.1507889112
652 Kelley, D.S., Karson, J.A., Früh-Green, G.L., Yoerger, D.R., Shank, T.M., Butterfield, D.A., Hayes, J.M.,
653 Schrenk, M.O., Olson, E.J., Proskurowski, G., Jakuba, M., Bradley, A., Larson, B., Ludwig, K.,

Glickson, D., Buckman, K., Bradley, A.S., Brazelton, W.J., Roe, K., Elend, M.J., Delacour, A., Bernasconi, S.M., Lilley, M.D., Baross, J.A., Summons, R.E., Sylva, S.P., 2005. A Serpentinite-Hosted Ecosystem: The Lost City Hydrothermal Field. Science 307, 1428–1434. https://doi.org/10.1126/science.1102556

Kempf, E.D., Hermann, J., 2018. Hydrogen incorporation and retention in metamorphic olivine during subduction: Implications for the deep water cycle. Geology 46, 571–574.

Klein, F., Bach, W., 2009. Fe–Ni–Co–O–S phase relations in peridotite–seawater interactions. J. Petrol. 50, 37–59.

Klein, F., Bach, W., Humphris, S.E., Kahl, W.-A., Jöns, N., Moskowitz, B., Berquó, T.S., 2014. Magnetite in seafloor serpentinite—Some like it hot. Geology 42, 135–138.

Klein, F., Bach, W., McCollom, T.M., 2013. Compositional controls on hydrogen generation during serpentinization of ultramafic rocks. Lithos 178, 55–69.

Klein, F., Grozeva, N.G., Seewald, J.S., 2019. Abiotic methane synthesis and serpentinization in olivine-hosted fluid inclusions. Proc. Natl. Acad. Sci. 116, 17666–17672.

Laird, J., Lanphere, M.A., Albee, A.L., 1984. Distribution of Ordovician and Devonian metamorphism in mafic and pelitic schists from northern Vermont. Am. J. Sci. 284, 376–413.

Laird, J., Trzcienski, W.E., Bothner, W.A., Cheney, J.T., Hepburn, J.C., 1993. High-pressure, Taconian, and subsequent polymetamorphism of southern Quebec and northern Vermont. Contrib. Dep. Univ. Mass. 67, 1–32.

Lamadrid, H.M., Rimstidt, J.D., Schwarzenbach, E.M., Klein, F., Ulrich, S., Dolocan, A., Bodnar, R.J., 2017. Effect of water activity on rates of serpentinization of olivine. Nat. Commun. 8, 1–9.

Li, L., Cartigny, P., Ader, M., 2009. Kinetic nitrogen isotope fractionation associated with thermal decomposition of NH3: Experimental results and potential applications to trace the origin of N2 in natural gas and hydrothermal systems. Geochim. Cosmochim. Acta 73, 6282–6297.

Majumdar, A.S., Hövelmann, J., Vollmer, C., Berndt, J., Mondal, S.K., Putnis, A., 2016. Formation of Mg-rich olivine pseudomorphs in serpentinized dunite from the Mesoarchean Nuasahi Massif, Eastern India: Insights into the evolution of fluid composition at the mineral–fluid interface. J. Petrol. 57, 3–26.

McCollom, T.M., 2016. Abiotic methane formation during experimental serpentinization of olivine. Proc. Natl. Acad. Sci. 113, 13965–13970.

Ménez, B., Pisapia, C., Andreani, M., Jamme, F., Vanbellingen, Q.P., Brunelle, A., Richard, L., Dumas, P., Réfrégiers, M., 2018. Abiotic synthesis of amino acids in the recesses of the oceanic lithosphere. Nature 564, 59–63. https://doi.org/10.1038/s41586-018-0684-z

Mével, C., 2003. Serpentinization of abyssal peridotites at mid-ocean ridges. Comptes Rendus Geosci. 335, 825–852.

Moody, J.B., 1976. Serpentinization: a review. Lithos 9, 125–138.

Nozaka, T., 2018. Compositional variation of olivine related to high–temperature serpentinization of peridotites: Evidence from the Oeyama ophiolite. J. Mineral. Petrol. Sci. 180420.

Nozaka, T., 2003. Compositional heterogeneity of olivine in thermally metamorphosed serpentinite from Southwest Japan. Am. Mineral. 88, 1377–1384.

Penniston-Dorland, S.C., Ferry, J.M., 2006. Development of spatial variations in reaction progress during regional metamorphism of micaceous carbonate rocks, northern New England. Am. J. Sci. 306, 475–524.

Plank, T., Manning, C.E., 2019. Subducting carbon. Nature 574, 343–352.

Plümper, O., John, T., Podladchikov, Y.Y., Vrijmoed, J.C., Scambelluri, M., 2017. Fluid escape from subduction zones controlled by channel-forming reactive porosity. Nat. Geosci. 10, 150–156. https://doi.org/10.1038/ngeo2865

Plümper, O., King, H.E., Vollmer, C., Ramasse, Q., Jung, H., Austrheim, H., 2012a. The legacy of crystal-plastic deformation in olivine: high-diffusivity pathways during serpentinization. Contrib. Mineral. Petrol. 163, 701–724.

Plümper, O., Piazolo, S., Austrheim, H., 2012b. Olivine pseudomorphs after serpentinized orthopyroxene record transient oceanic lithospheric mantle dehydration (Leka Ophiolite Complex, Norway). J. Petrol. 53, 1943–1968.
Rouméjon, S., Andreani, M., Früh-Green, G.L., 2019. Antigorite crystallization during oceanic retrograde serpentinization of abyssal peridotites. Contrib. Mineral. Petrol. 174, 60.
Rumble III, D., Hoering, T.C., 1986. Carbon isotope geochemistry of graphite vein deposits from New Hampshire, USA. Geochim. Cosmochim. Acta 50, 1239–1247.
Scambelluri, M., Müntener, O., Hermann, J., Piccardo, G.B., Trommsdorff, V., 1995. Subduction of water into the mantle: history of an Alpine peridotite. Geology 23, 459–462.
Scambelluri, M., Strating, E.H., Piccardo, G.B., Vissers, R.L.M., Rampone, E., 1991. Alpine olivine-and titanian clinohumite-bearing assemblages in the Erro-Tobbio peridotite (Voltri Massif, NW Italy). J. Metamorph. Geol. 9, 79–91.
Scambelluri, M., Tonarini, S., 2012. Boron isotope evidence for shallow fluid transfer across subduction zones by serpentinized mantle. Geology 40, 907–910.
Schrenk, M.O., Brazelton, W.J., Lang, S.Q., 2013. Serpentinization, carbon, and deep life. Rev. Mineral. Geochem. 75, 575–606.
Schwartz, S., Guillot, S., Reynard, B., Lafay, R., Debret, B., Nicollet, C., Lanari, P., Auzende, A.L., 2013. Pressure–temperature estimates of the lizardite/antigorite transition in high pressure serpentinites. Lithos 178, 197–210.
Seyfried Jr, W.E., Foustoukos, D.I., Fu, Q., 2007. Redox evolution and mass transfer during serpentinization: An experimental and theoretical study at 200 C, 500 bar with implications for ultramafic-hosted hydrothermal systems at Mid-Ocean Ridges. Geochim. Cosmochim. Acta 71, 3872–3886.
Shen, T., Hermann, J., Zhang, L., Lü, Z., Padrón-Navarta, J.A., Xia, B., Bader, T., 2015. UHP metamorphism documented in Ti-chondrodite-and Ti-clinohumite-bearing serpentinized ultramafic rocks from Chinese southwestern Tianshan. J. Petrol. 56, 1425–1458.
Sleep, N.H., Bird, D.K., 2007. Niches of the pre-photosynthetic biosphere and geologic preservation of Earth's earliest ecology. Geobiology 5, 101–117.
Stanley, R.S., Roy, D.L., Hatch, N.L., Knapp, D.A., 1984. Evidence for tectonic emplacement of ultramafic and associated rocks in the pre-Silurian eugeoclinal belt of western New England; vestiges of an ancient accretionary wedge. Am. J. Sci. 284, 559–595. https://doi.org/10.2475/ajs.284.4-5.559
Sverjensky, D.A., Harrison, B., Azzolini, D., 2014. Water in the deep Earth: the dielectric constant and the solubilities of quartz and corundum to 60 kb and 1200 C. Geochim. Cosmochim. Acta 129, 125–145.
Touret, J.L.R., 2001. Fluids in metamorphic rocks. Lithos 55, 1–25.
Trommsdorff, V., Evans, B.W., 1974. Alpine metamorphism of peridotitic rocks. Schweiz Min Pet Mitt 54, 333–352.
Van Baalen, M.R., Mossman, B.T., Gunter, M.E., Francis, C.A., 2009. Environmental Geology of Belvidere Mt.
Vitale Brovarone, A., Martinez, I., Elmaleh, A., Compagnoni, R., Chaduteau, C., Ferraris, C., Esteve, I., 2017. Massive production of abiotic methane during subduction evidenced in metamorphosed ophicarbonates from the Italian Alps. Nat. Commun. 8, 14134.
Vitale Brovarone, A., Sverjensky, D.A., Piccoli, F., Ressico, F., Giovannelli, D., Daniel, I., 2020. Subduction hides high-pressure sources of energy that may feed the deep subsurface biosphere. Nat. Commun. 11, 1–11.
Viti, C., Mellini, M., Rumori, C., 2005. Exsolution and hydration of pyroxenes from partially serpentinized harzburgites. Mineral. Mag. 69, 491–507.
Wada, I., Wang, K., He, J., Hyndman, R.D., 2008. Weakening of the subduction interface and its effects on surface heat flow, slab dehydration, and mantle wedge serpentinization. J. Geophys. Res. Solid Earth 113.

Wenner, D.B., Taylor, H.P., 1974. D/H and O18/O16 studies of serpentinization of ultramaflc rocks. Geochim. Cosmochim. Acta 38, 1255–1286.
Wenner, D.B., Taylor, H.P., 1971. Temperatures of serpentinization of ultramafic rocks based on O 18/O 16 fractionation between coexisting serpentine and magnetite. Contrib. Mineral. Petrol. 32, 165–185.
Wolery, Tj., Jarek, R.L., 2003. Software user's manual: EQ3/6, version 8.0. Softw. Doc. 8–0.
Zhang, S., Ague, J.J., Vitale Brovarone, A., 2018. Degassing of organic carbon during regional metamorphism of pelites, Wepawaug Schist, Connecticut, USA. Chem. Geol. 490, 30–44. https://doi.org/10.1016/j.chemgeo.2018.05.003

Fig. 1*: A: Simplified geological map of Vermont, modified from Hibbard et al., (2006). B: Simplified bedrock geologic map of the Belvidere Mountain Complex and the surrounding formations. Modified after Hibbard et al., (2006). Units description from Hibbard et al., (2006) and Gale, (2007).*

Fig. 2*: A-B: Photographs of the Belvidere serpentinized peridotite in outcrop. C: Weakly serpentinized dunite (samples V18-2a and V18-2b). D: Serpentinized dunite, with boudinaged meta-gabbro (samples V18-3a and V18-3b).*

Fig. 3*: A: Photomicrograph of a partially serpentinized dunite. B: Partial replacement of primary chromian spinel by magnetite and chlorite. C: Partial replacement of olivine by antigorite. D: Inferred primary orthopyroxene being pseudomorphically replaced by metamorphic olivine. See also Figure 5B. E: Photomicrograph of a pyroxenite layer included in the Belvidere peridotite. The photomicrograph shows radial diopside aggregate pseudomorphic on primary clinopyroxene. Partially serpentinized olivine is also visible. F: Magnetite-rich diopside pseudomorphosis on primary clinopyroxene. Note the growth of metamorphic olivine at the rim of the clinopyroxene site. See Figure 5A for SEM-based backscattered electron image. G: Metamorphic diopside replacing primary clinopyroxene. In this case, note the growth of metamorphic olivine along fractures cutting the pseudomorphosis. See Figure 5F for SEM-based backscattered electron image. H: Relict of metamorphic olivine pseudomorphic on primary clinopyroxene. The metamorphic olivine is then partially replaced by serpentine + brucite + magnetite. A-D: Sample V18-2b, E-G: Sample V18-3a; H: sample V18-B3. P-Ol: primary olivine, M-Ol: metamorphic olivine, Atg: antigorite, Chl: chlorite, Mgt: magnetite, Di: diopside, Chr: chromite, Br: brucite, Ctl: chrysotile.*

***Fig. 4**: Raman spectra of solid phases. A: Primary olivine. B Antigorite overgrowing primary olivine. C: Antigorite core (Atg1) and rim (Atg2) (see Fig. 5A). D: Brucite.*

***Fig. 5**: SEM-BSE images of samples V18-2b,V18-3a and V18-B3. A: Microstructural patterns of serpentinization. Two generations of serpentine can be observed based on the BSE contract, a bright core (Atg1) and a dark rim (Atg2). Note also the striped zonation of primary olivine and the formation of metamorphic olivine. B: Replacement of an inferred primary orthopyroxene crystal by metamorphic olivine. The close-up shows the preservation of clinopyroxene relicts interpreted as exsolutions inside the former orthopyroxene. C: Formation of at the expense of metamorphic. D: Composite aggregate of Fe-Ni and Fe-Cu-Ni alloys and Ni sulphide. E: Growth of metamorphic olivine around a diopside-rich primary clinophyroxene pseudomorphosis. A primary chromina spinel partially converted into magnetite can also be observed. F: Metamorphic diopside replacing primary clinopyroxene. Note the presence of antigorite + metamorphic olivine ± magnetite along the fractures. In this case, metamorphic olivine occupies the centre of the fractures and is not in contact with diopside, whereas the metamorphic olivine rimming the primary clinopyroxene site is in contact with it. G: Metamorphic olivine growing at the expense of metamorphic diopside (former primary clinopyroxene). The microstructure suggests the former presence of serpentine needles replacing the clinopyroxene and successively replaced by metamorphic olivine. Both Atg1 and Atg2 antigorite generations are present. H: Relict of metamorphic olivine formed at the expense of a primary orthopyroxene site in V18-3b. The metamorphic olivine is partially converted into brucite + serpentine. P-Ol: primary olivine M-Ol: metamorphic olivine Px: pyroxene Di: diopside Mtg: magnetite Chr: chromite Atg: antigorite Br: brucite Ctl: chrysotile NiFeS: nickel and iron sulphite. The presence of antigorite was confirmed by Raman spectroscopy.*

***Fig. 6**: Mg# versus MnO (wt%) diagram showing the compositional variation of primary and metamorphic olivine. The Mn-richest cluster of metamorphic olivine belongs to sample V18-B3 (fully serpentinized peridotite). Background data from Arai et al., (2012); Dandar et al., (2019); Debret et al., (2013); Iyer et al., (2008); Nozaka, (2018); Plümper et al., (2012b); Scambelluri et al., (1995); Shen et al., (2015).*

***Fig. 7**: Photomicrographs of methane-rich fluid inclusion trails in olivine from sample V18-2a. Black arrows indicate fluid inclusion trails. A: Inclusion trail being cut by antigorite veinlets. B: Inclusion trail limited by antigorite veins. C: Secondary trail of fluid inclusions propagating from an antigorite veinlet. D: Photomicrograph showing a fluid-inclusion-rich olivine aggregate. E: Close up of the methane-rich fluid inclusions. F: Close up of a graphite bearing fluid inclusion (red arrow), as confirmed by Raman spectroscopy in (Fig. 8B).*

***Fig. 8**: Raman spectra of fluid inclusions and step-daughter solid phases. A: Inclusion showing a marked CH_4 band and minor peaks of N_2 NH_3 and S-H bond. Lizardite and brucite O-H bands are also observed. B: Graphite in fluid inclusions (see Fig. 6D). C: Methane-rich fluid inclusion with a close up of O-H bonds of lizardite and brucite.*

***Fig. 9**: Calculated molar fraction of CH_4, N_2, H_2S and NH_3 from Raman scattering cross-section and the instrumental efficiency of each species. See Frezzotti et al., (2012) for methodology.*

***Fig. 10**: Thermodynamic modelling of HP serpentinization of dunite and related mineralogical and fluid evolution. A: Mineralogical evolution during serpentinization at 450 °C and 1 GPa. Representative microstructures of the main reaction steps are proposed as observed in the natural samples. B: Evolution of the nitrogen and sulphur fluid speciation as a function of the reaction progress presented in A. C: Evolution of the fO_2 and H_2, CH_4, and CO_2 concentrations in the fluid as a function of the reaction progress presented in A.*

Fig. 11*: Reconstruction of the mineralogical evolution of the BMC partially serpentinized peridotite. An early step of serpentinization is proposed based on the needle-like growth of metamorphic olivine on primary clinopyroxene, suggesting the presence of serpentine prior to the formation of metamorphic olivine. The successive growth of antigorite at the expense of both primary and metamorphic olivine constrains the main serpentinization event to metamorphic conditions. Finally, a late serpentinization event is proposed based on the growth of brucite + antigorite + chrysotile on relict metamorphic. Chr : chromite, P-Ol : primary olivine, M-Ol : metamorphic olivine, Opx : primary orthopyroxene, Cpx : primary clinopyroxene, Chl : chlorite, Mgt : magnetite, Atg : antigorite, Di : diopside, Brc : brucite, Ctl : chrysotile.*

Fig. 12*: Stability field of serpentine type minerals and olivine, modified from Guillot et al., (2015) (see references therein for details on the main reactions). The retrograde P-T path of BMC from Honsberger, (2015) is also shown for reference. Atg : antigorite, Brc : brucite; Ctl : chrysotile; Ilm : ilmenite; Ol : olivine; Tlc : talc; Ticl : titanian clinohumite.*

Figure 1

Click here to access/download;Figure;Fig1.tif

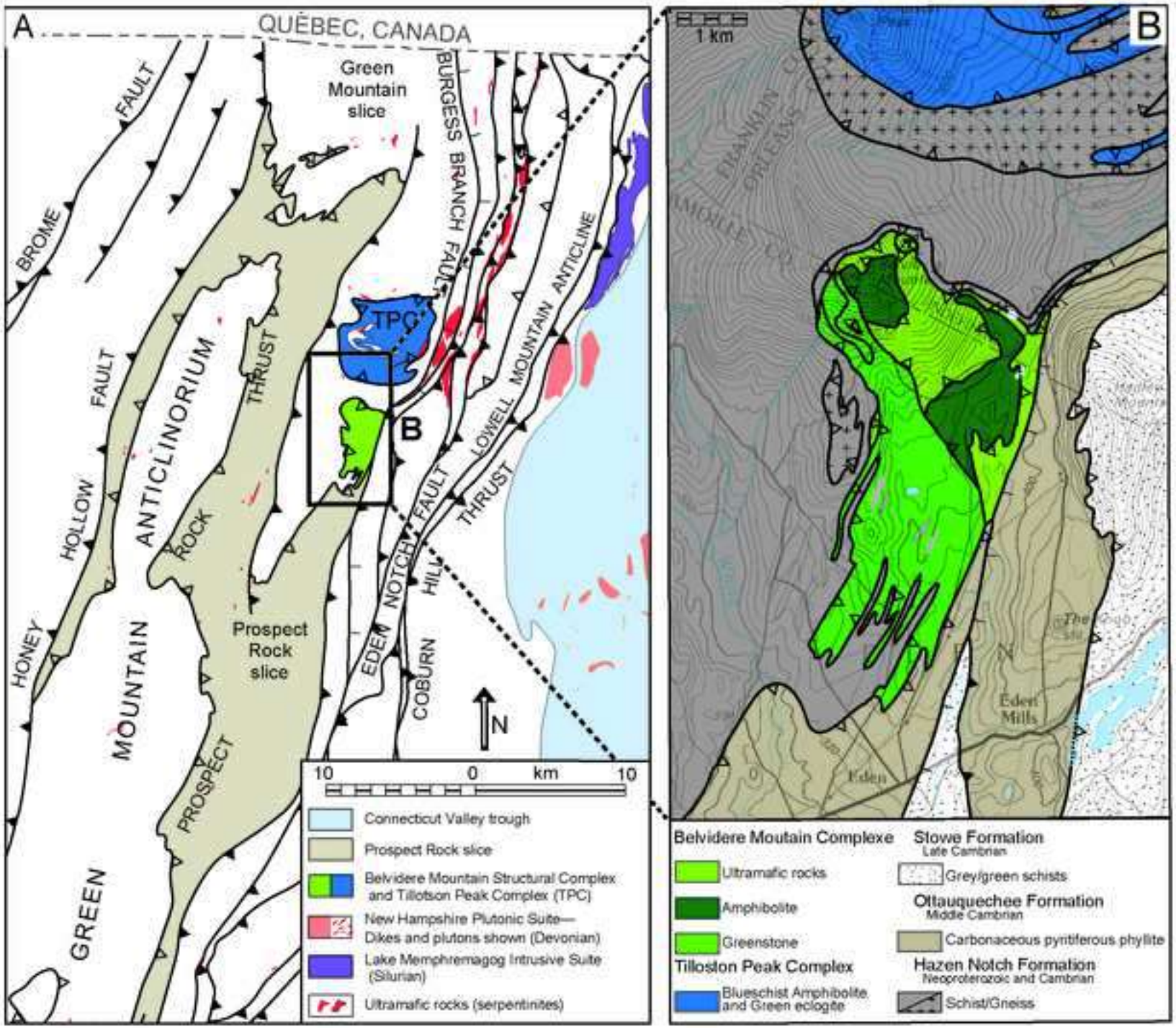

Figure 2

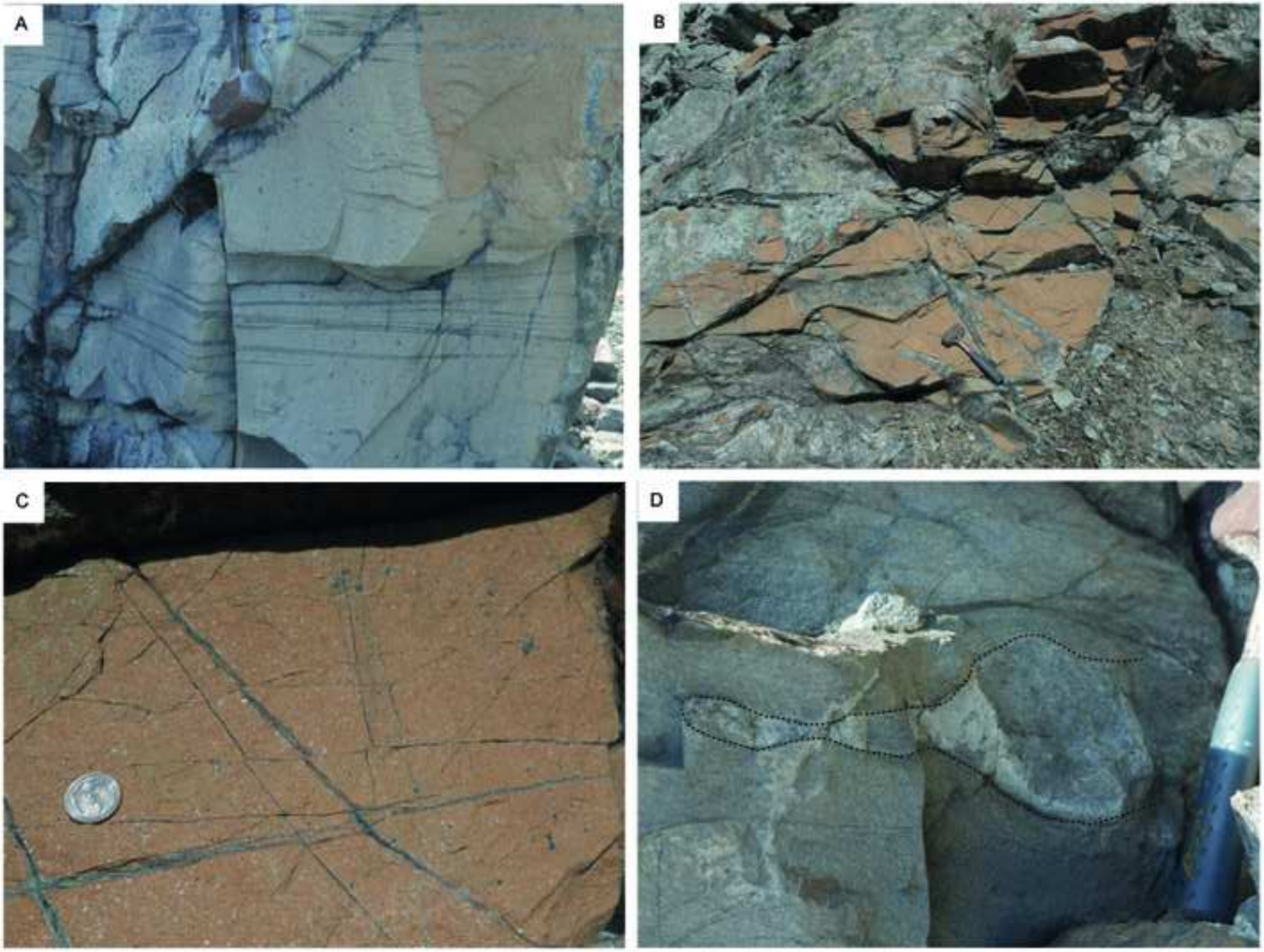

Figure 3

Click here to access/download;Figure;Fig3.tif

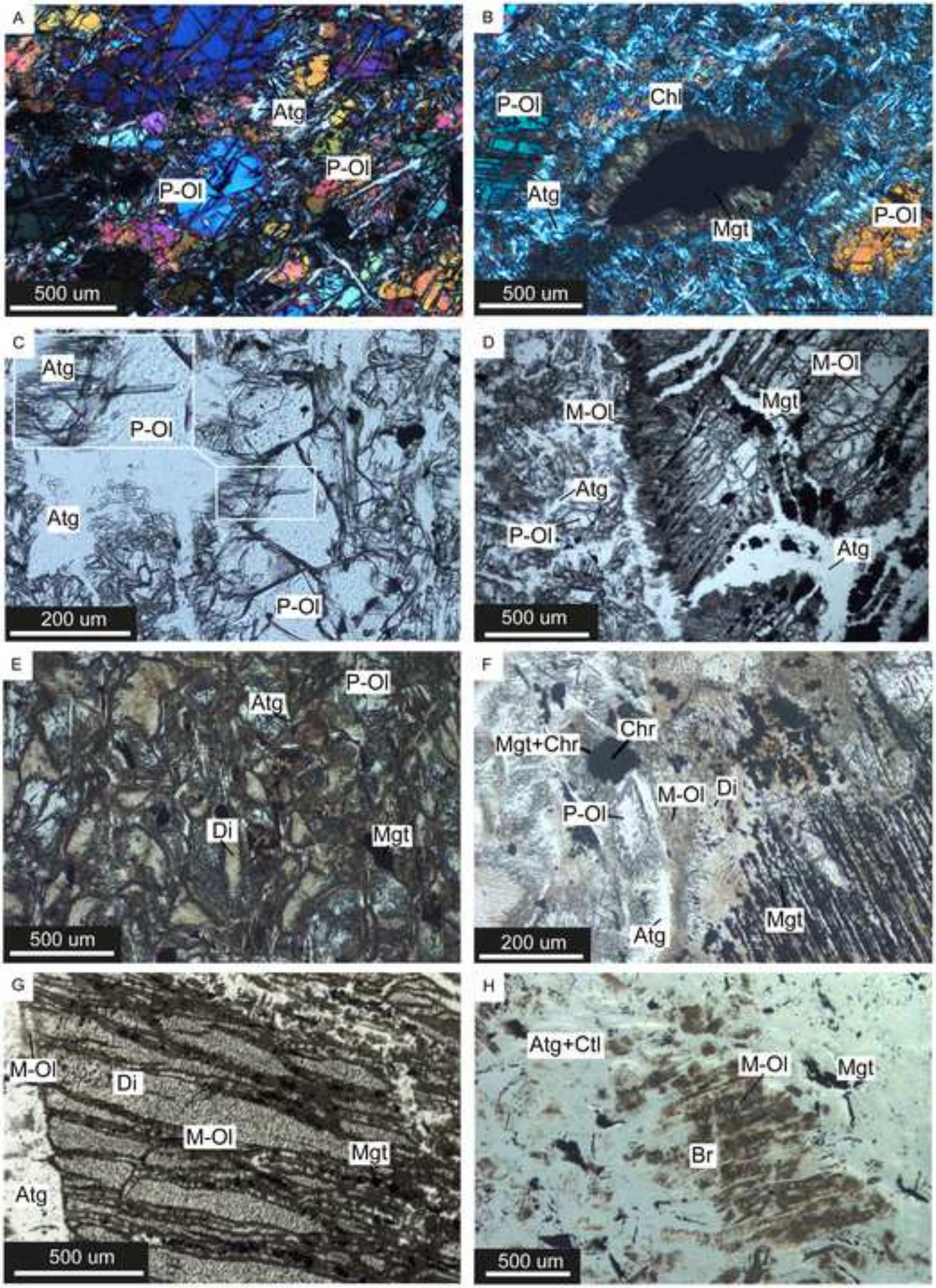

Figure 4

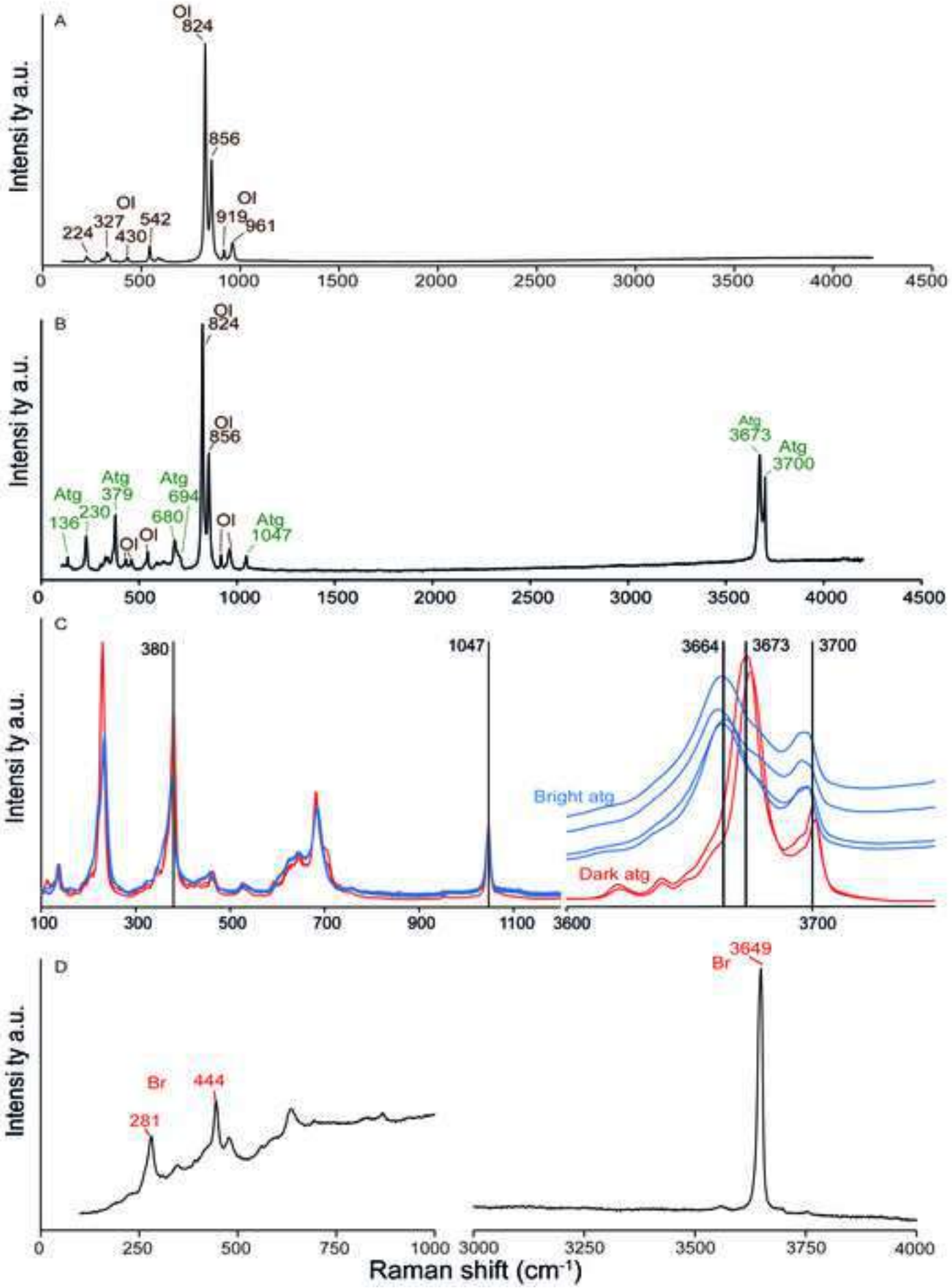

Figure 5

Click here to access/download;Figure;Fig5.tif

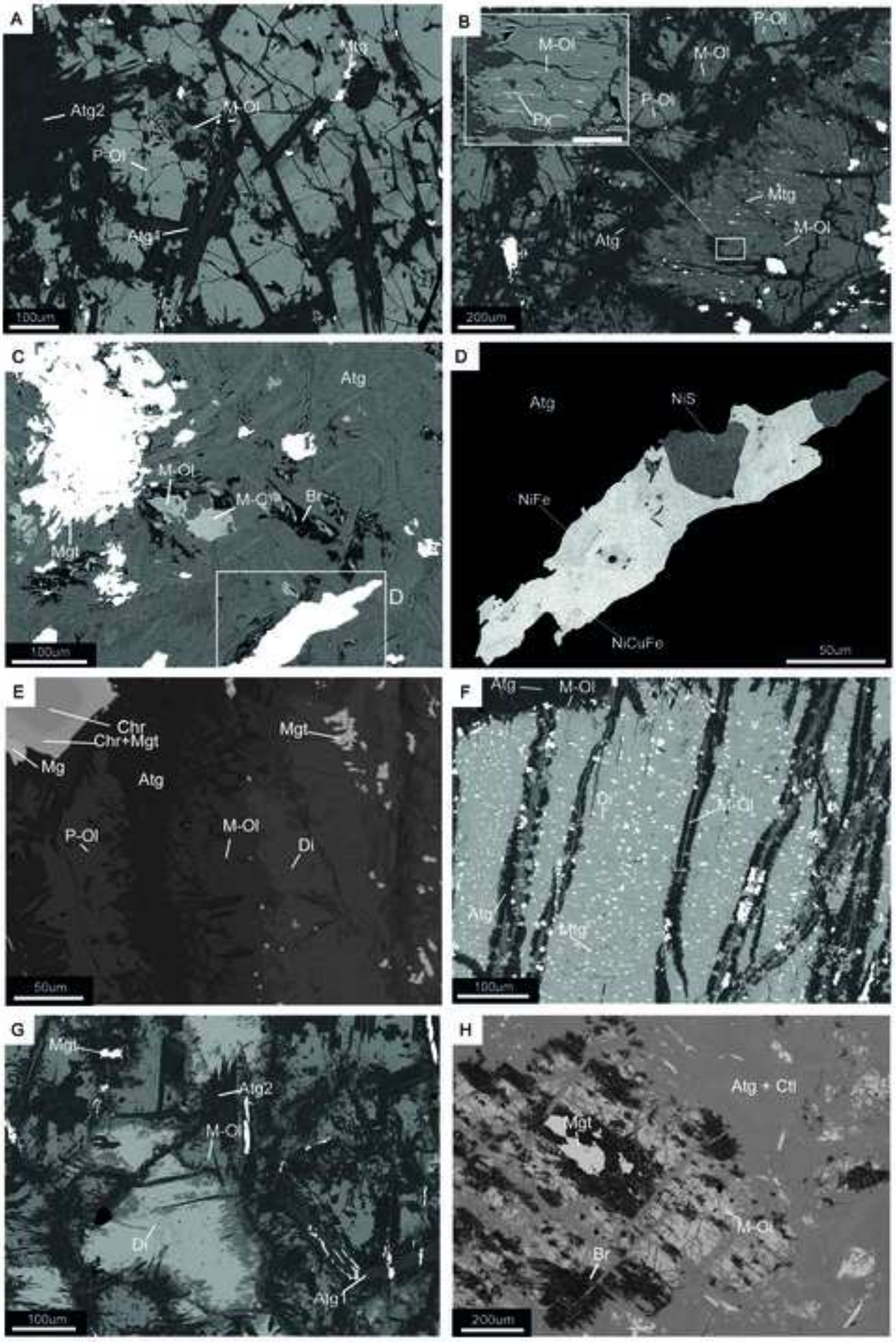

Figure 6

Click here to access/download;Figure;Fig6.tif

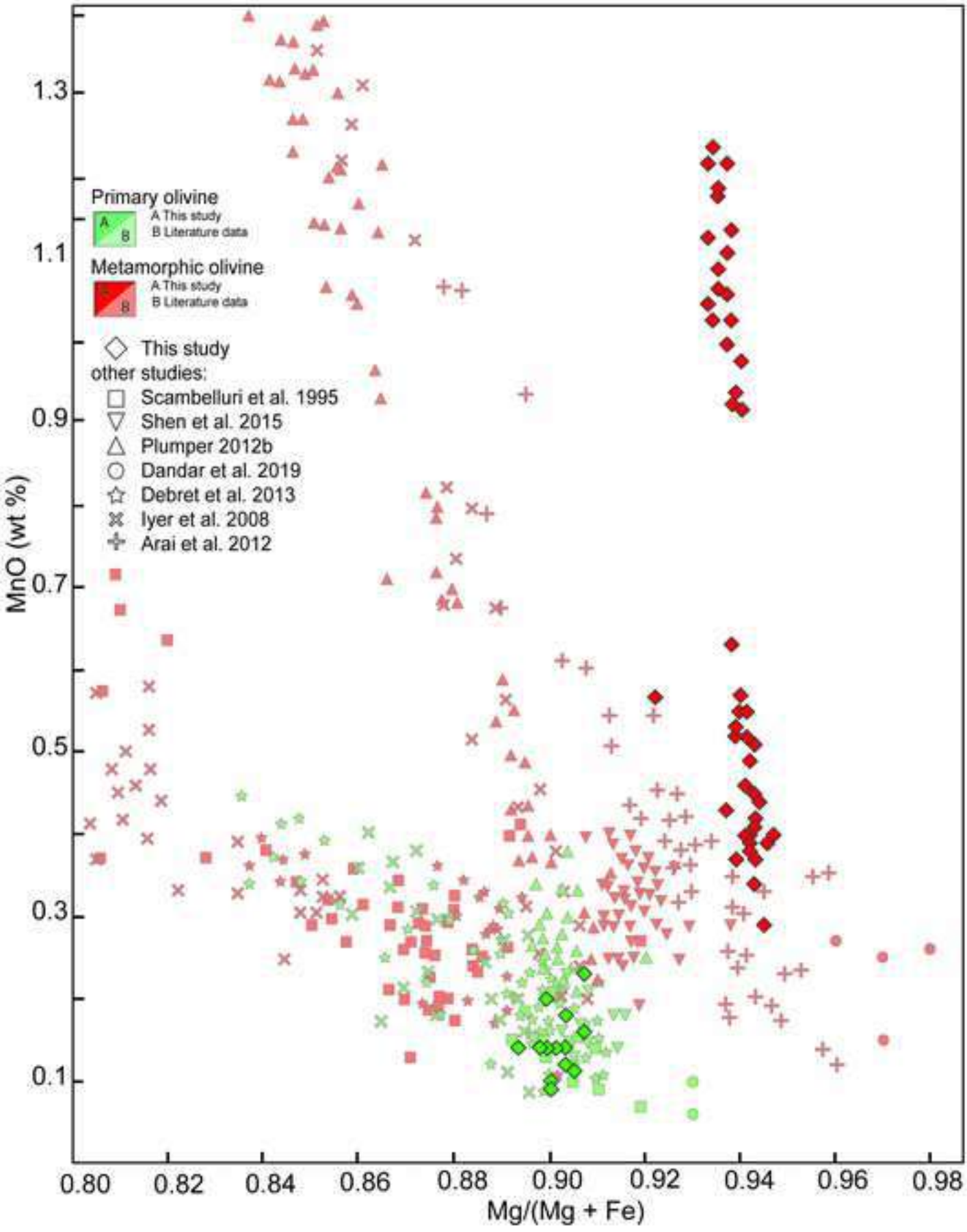

Figure 7

Click here to access/download;Figure;Fig7.tif

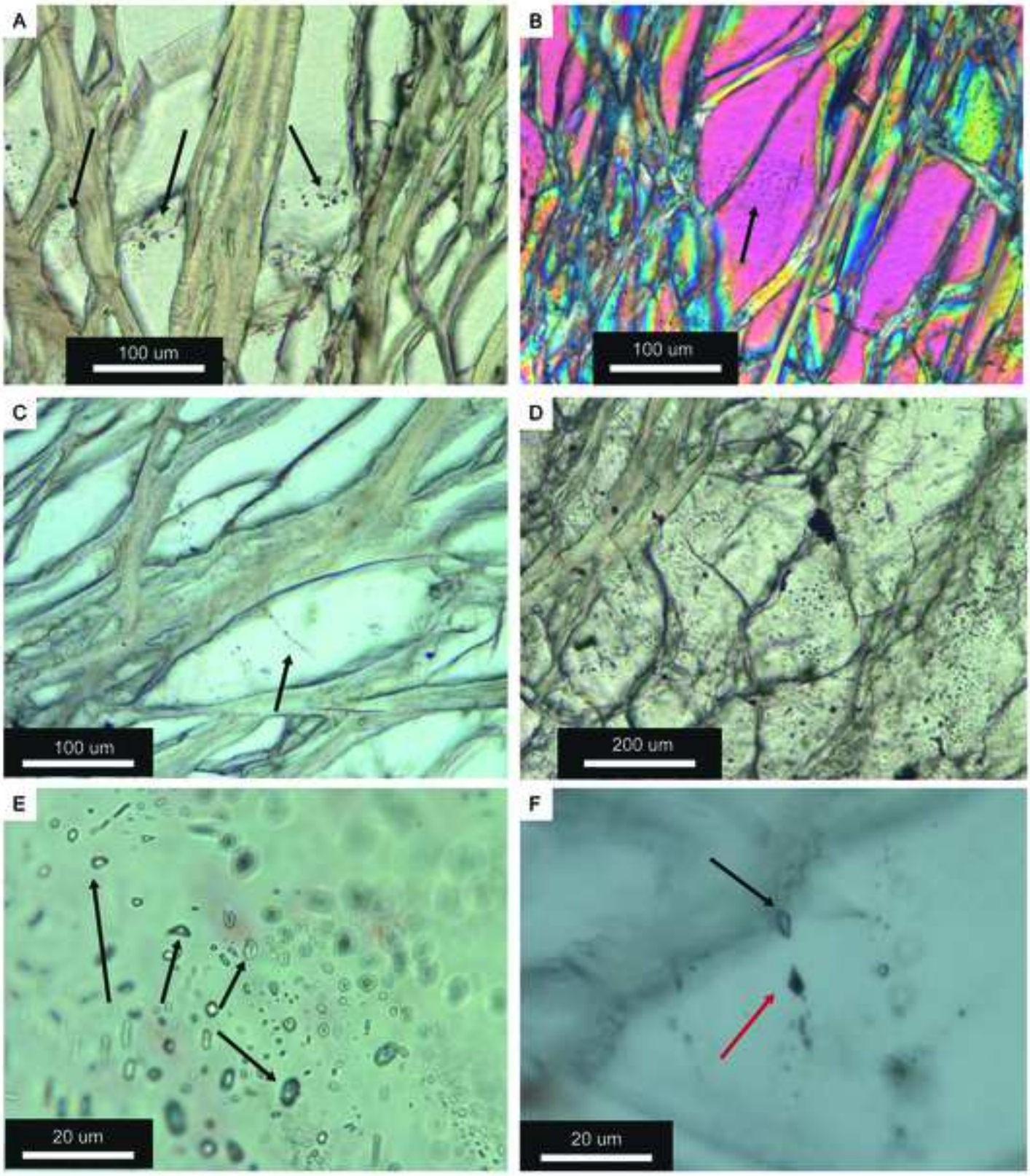

Figure 8

Click here to access/download;Figure;Fig8.tif

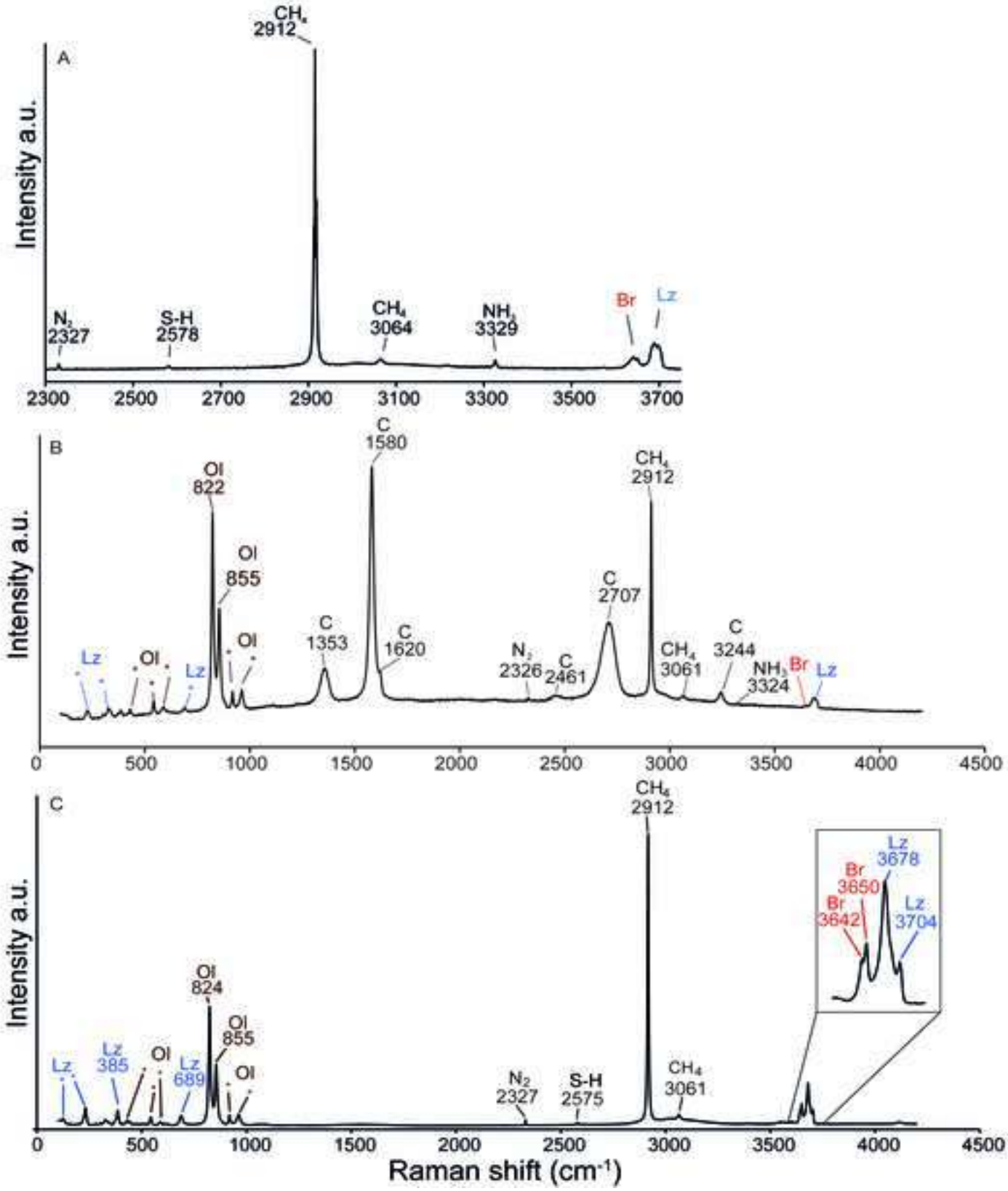

Figure 9

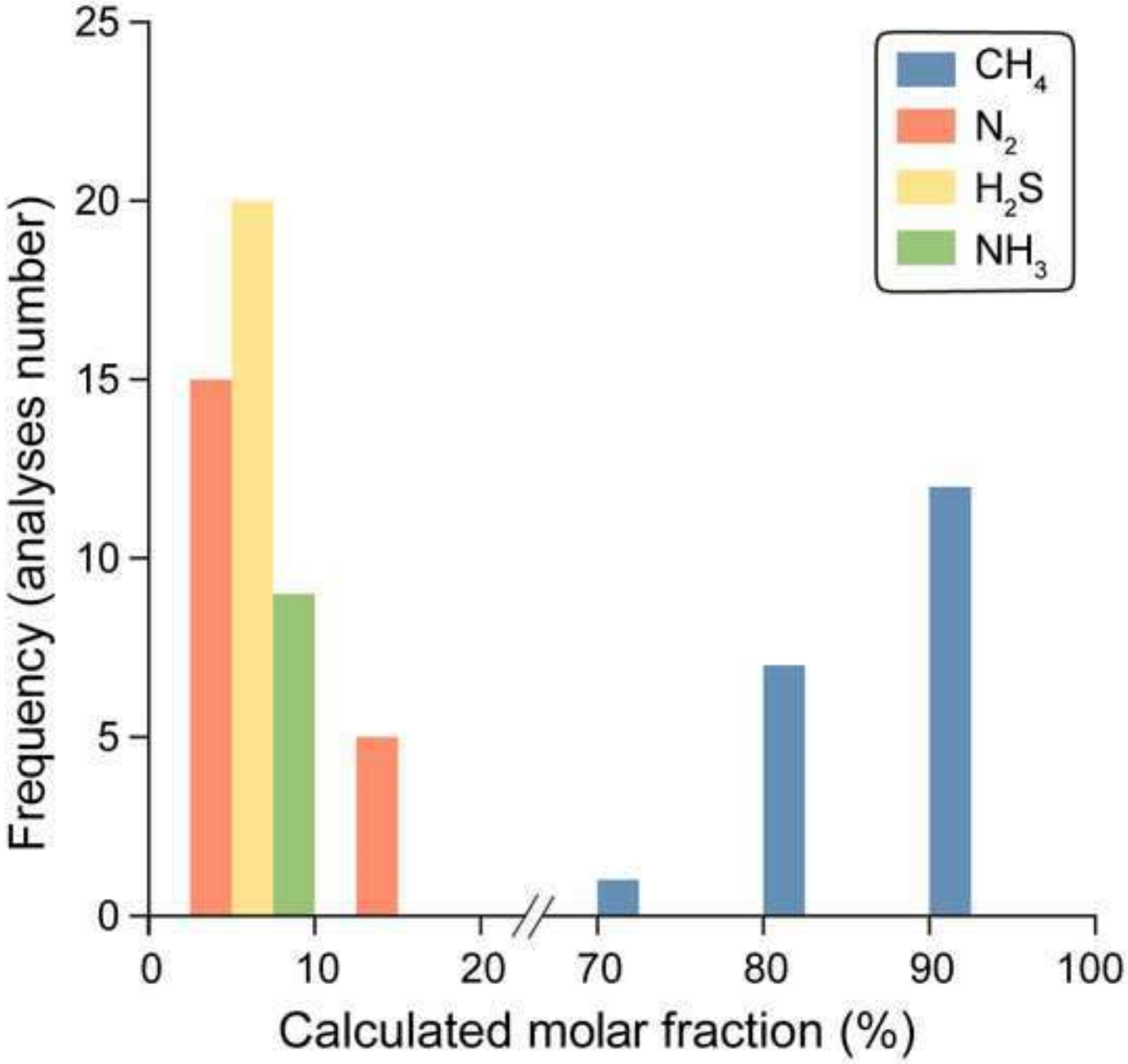

Figure 10

Click here to access/download;Figure;Fig10.tif

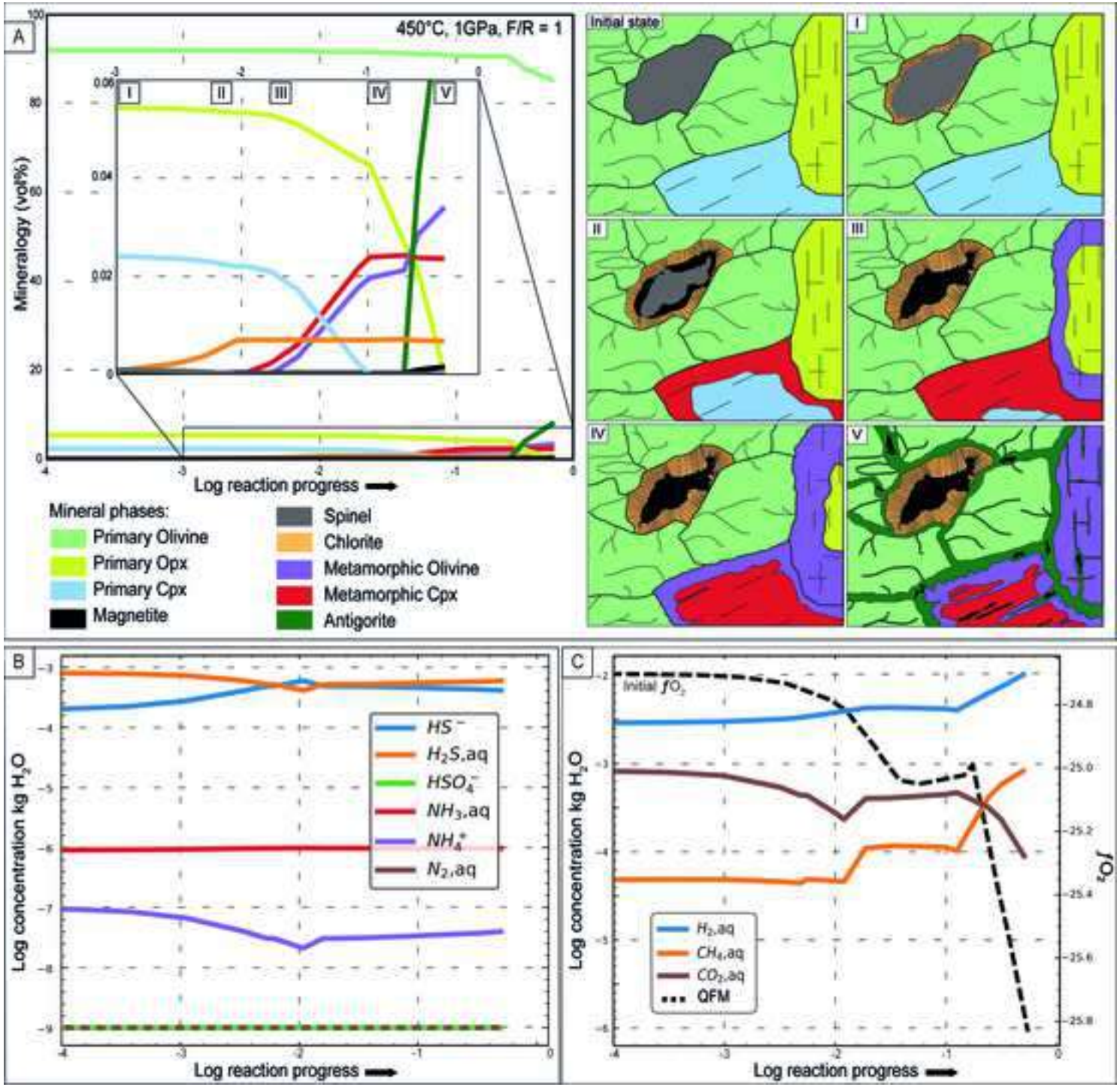

Figure 11

Click here to access/download;Figure;Fig11.tif

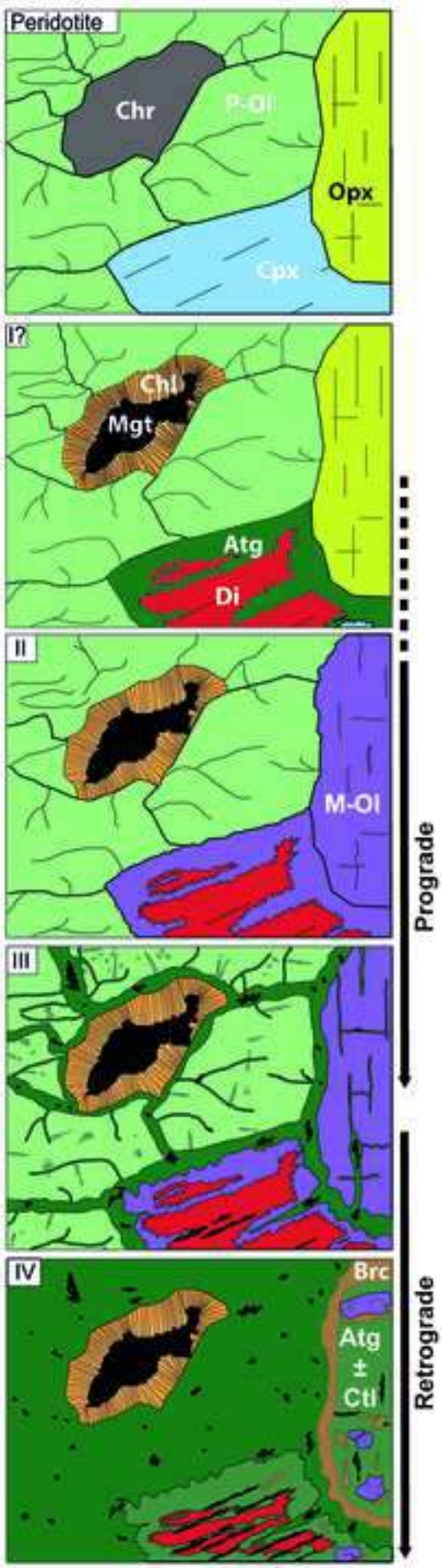

Figure 12

Click here to access/download;Figure;Fig12.tif

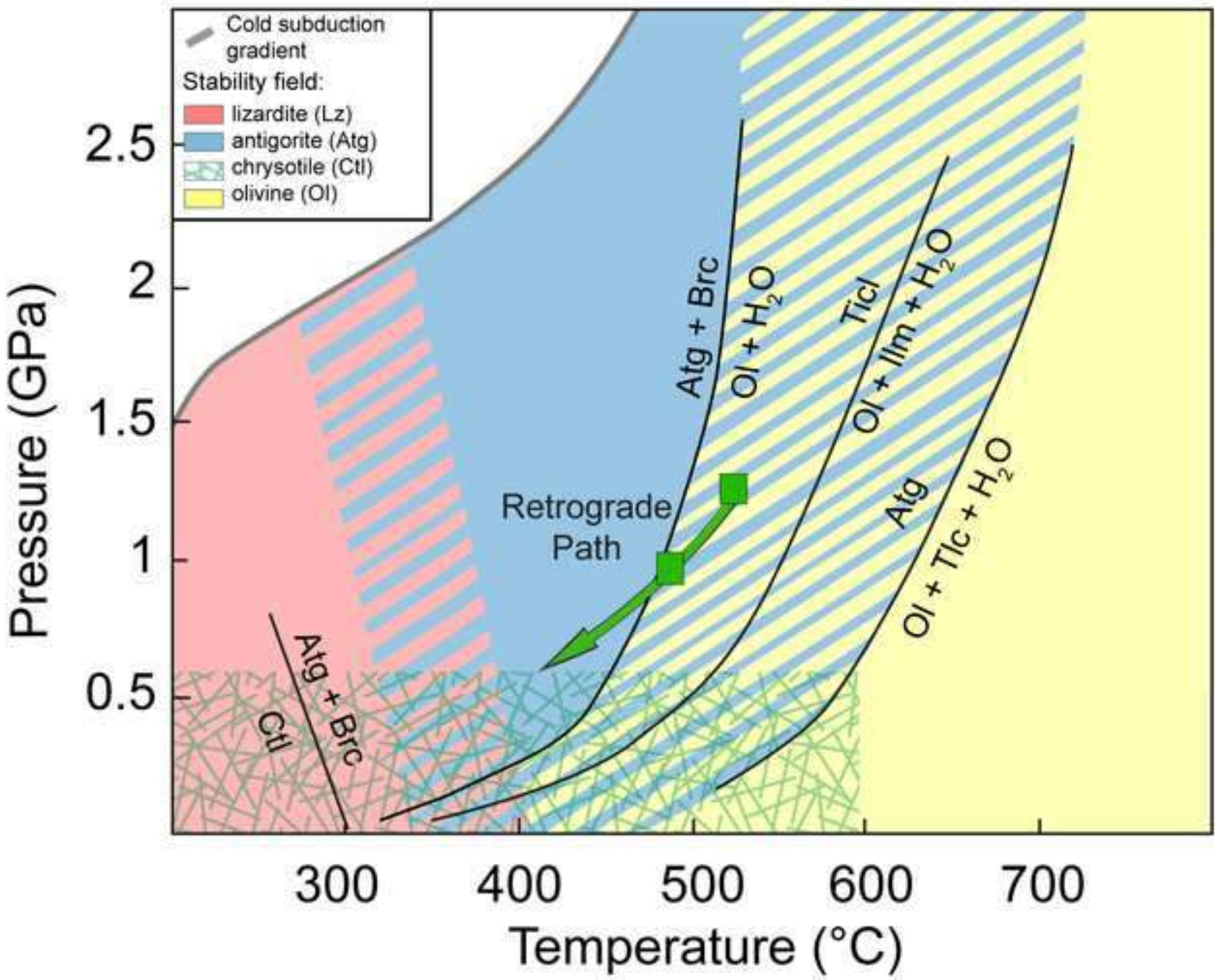

1 **Table 1**

MicroProbe analysis. Absence of SD value when n>1 indicates SD<0.01. *EDS analyses normalized at 100.

Minerals	**Primary Olivine**		**Metamorphic Olivine**			**Pyroxene**	**Serpentine (Bright core)**		**Serpentine (Matrix)**		**Chlorite**	
Sample	**V18-2b**	**V18-3a**	**V18-2b**	**V18-3a**	**V18-B3***	**V18-3a**	**V18-2b**	**V18-3a**	**V18-2b**	**V18-3a**	**V18-2b**	**V18-3a**
(n)	14	11	28	15	25	20	6	2	9	4	11	1
SiO_2	40.91 (0.25)	40.83 (0.46)	41.31 (0.49)	41.95 (0.63)	42.00 (0.12)	54.96 (0.98)	42.87 (1.21)	43.41 (0.1)	44.15 (0.17)	43.1 (1.35)	32.61 (1.34)	32.03
TiO_2	0.01 (0.01)	0.02 (0.02)	0.02 (0.01)	0.02 (0.02)		0.03 (0.02)	0.01 (0.01)	0.02 (0.01)	0.02 (0.01)	0 (0)	0.02 (0.02)	0.00
Al_2O_3	0.01 (0.01)	0.01 (0.01)	0.01 (0.02)	0.04 (0.09)		0.15 (0.11)	1.77 (1.22)	1.45 (0.78)	0.52 (0.21)	0.47 (0.26)	14.34 (2.39)	11.78
Cr_2O_3	0.01 (0.02)	0.01 (0.02)	0.06 (0.18)	0.04 (0.03)		0.17 (0.11)	0.61 (0.85)	0.25 (0.19)	0.13 (0.09)	0.1 (0.1)	1.07 (0.56)	4.07
FeO (tot)	8.97 (0.34)	7.93 (0.22)	4.83 (0.30)	5.05 (0.57)	4.71 (0.19)	0.76 (0.16)	2.60 (0.26)	1.58 (0.27)	1.35 (0.22)	1.2 (0.29)	3.31 (0.46)	2.79
MnO	0.15 (0.04)	0.12 (0.06)	0.45 (0.08)	0.37 (0.06)	1.02 (0.18)	0.05 (0.03)	0.04 (0.02)	0.05 (0.05)	0.04 (0.02)	0.02 (0.02)	0.06 (0.10)	0.07
NiO	0.38 (0.03)	0.49 (0.06)	0.43 (0.07)	0.39 (0.06)	0.46 (0.08)	0.03 (0.03)	0.16 (0.02)	0.18 (0.06)	0.15 (0.04)	0.19 (0.02)	0.22 (0.05)	0.24
ZnO	0.04 (0.04)	0.03 (0.04)	0.03 (0.04)	0.03 (0.04)		0.01 (0.02)					0.02 (0.04)	0.00
MgO	50.23 (0.22)	50.91 (0.22)	52.8 (0.64)	51.8 (1.57)	51.80 (0.28)	18.75 (1.15)	37.97 (1.30)	39.81 (0.59)	39.6 (0.77)	40.07 (0.61)	34.34 (1.11)	35.08
CaO	0.02 (0.01)	0.01 (0.02)	0.02 (0.02)	0.25 (0.37)		24.87 (1.43)	0.02 (0.02)	0.05 (0.04)	0.02 (0.02)	0.02 (0.01)	0.02 (0.01)	0.05
Na_2O	0.09 (0.22)	0.01 (0.01)	0.02 (0.02)	0.01 (0.01)		0.04 (0.02)					0.02 (0.03)	0.03
K_2O	0.01 (0.02)	0.01 (0.01)	0.01 (0.01)	0.01 (0.01)		0.01 (0.01)					0.02 (0.02)	0.02
Total,	100.82 (0.36)	100.37 (0.70)	100.06 (1.10)	99.96 (1.63)	100	99.83 (1.12)	86.2 (0.63)	86.93 (0.4)	86.07 (0.82)	85.25 (1.66)	86.14 (0.65)	86.17
Cations												
Si	0.990	0.988	0.991	1.012	1.013	1.989	1.984	2.010	2.044	1.995	6.232	6.165
Ti	0.000	0.000	0.000	0.000		0.001	0.000	0.001	0.001	0.000	0.004	0.000
Al	0.000	0.000	0.000	0.001		0.006	0.091	0.079	0.028	0.026	3.229	2.672
Cr	0.000	0.000	0.001	0.001		0.005	0.026	0.009	0.005	0.004	0.162	0.619
Fe^{2+} (tot)	0.181	0.161	0.097	0.102	0.095	0.023	0.104	0.061	0.052	0.046	0.529	0.404
Mn	0.003	0.003	0.009	0.008	0.021	0.002	0.001	0.002	0.002	0.001	0.010	0.012
Ni	0.007	0.010	0.008	0.008	0.009	0.001	0.006	0.007	0.006	0.007	0.034	0.037
Zn	0.001	0.001	0.000	0.001		0.000					0.003	0.000
Mg	1.812	1.837	1.891	1.861	1.862	1.012	2.486	2.747	2.733	2.765	9.782	10.063
Ca	0.000	0.000	0.001	0.006		0.964	0.001	0.002	0.001	0.001	0.003	0.011
Na	0.004	0.000	0.001	0.000		0.003					0.007	0.012
K	0.000	0.000	0.000	0.000		0.000					0.005	0.005
Mg#	0.91	0.92	0.95	0.95	0.95	0.98	0.94	0.96	0.97	0.97	0.95	0.96

Mg# = Mg/(Mg+ΣFe)

2

Table 2

MicroProbe analysis. Absence of SD value when n>1 indicates SD<0.01

Minerals	**Spinel (nucleus)**	**Spinel (intermediate)**	**Magnetite (rim)**	**Magnetite (mesh and veins)**		**Brucite**
Sample	**V18-3a**	**V18-3a**	**V18-3a**	**V18-3a**	**V18-2b**	**V18-2b**
(n)	7	7	7	1	4	10
SiO_2	0.02 (0.02)	0.03 (0.01)	0.06 (0.07)	0.07	0.05 (0.03)	0.78 (2.20)
TiO_2	0.09 (0.02)	0.23 (0.05)	0.03 (0.02)	0.04	0.01 (0.01)	0.01
Al_2O_3	12.63 (0.94)	3.87 (1.34)	0.00	0.03	0.01 (0.01)	0.01 (0.01)
Cr_2O_3	47.51 (0.57)	41.6 (1.29)	1.87 (1.16)	0.01	0.02 (0.02)	0.04 (0.05)
FeO	34.12 (1.1)	48.32 (2.02)	91.45 (0.75)	92.44	92.57 (0.28)	2.91 (0.18)
MnO	0.34 (0.04)	0.95 (0.36)	0.16 (0.03)	0.12	0.19 (0.05)	0.22 (0.04)
NiO	0.09 (0.02)	0.27 (0.05)	1.05 (0.1)	1.11	0.82 (0.09)	0.38 (0.09)
ZnO	0.49 (0.08)	0.3 (0.1)	0.04 (0.06)	0.10	0.04 (0.08)	0.01 (0.02)
MgO	5.99 (0.32)	3.37 (0.22)	0.71 (0.09)	0.62	0.82 (0.19)	75.88 (3.93)
CaO	0.01 (0.01)	0.00	0 (0.01)	0.00	0.00	0.02 (0.03)
Na_2O	0.03 (0.04)	0.02 (0.02)	0.03 (0.03)	0.03	0.02 (0.04)	0.02 (0.02)
K_2O	0.00	0.01 (0.01)	0 (0.01)	0.01	0.00	0.01 (0.01)
Total	101.4 (0.56)	99.03 (0.6)	95.46 (0.5)	94.63	94.56 (0.45)	80.33 (2.70)
Cr#	0.79(0.01)	0.92(0.2)	1.00			

Cr# = Cr/(Al+Cr)

Table 3

MicroProbe analysis of alloys

Sample	**V18-2b**						**V18-3a**		
Alloy	**NiFeCu**	**NiS**	**NiS**	**NiS**	**NiFeCu**	**NiFeCu**	**NiS**	**NiS**	**NiS**
S		24.06	24.25	24.12			24.59	24.52	24.50
Fe	12.21	0.9	0.51	1.35	13.35	20.07	0.84		0.95
Pb				0.13			0.18		
Ni	86.23	72.68	72.71	73.55	86.05	80.03	72.97	72.85	73.30
Cu	1.94				1.75	1.49			
Total:	100.45	97.9	97.59	99.18	101.28	101.71	98.70	97.72	99.04

Table 4

Calculated partition coefficient between antigorite and olivine for Mg and Mn

	K_D Mg		**K_D Mn**	
Calculated K_D	**V18-2**	**V18-3b**	**V18-2**	**V18-3b**
Atg1 / P-Ol	0.25	0.14	0.42	0.54
Atg2 / P-Ol	0.11	0.11	0.42	0.27
Atg1 / M-Ol	0.49	0.23	0.14	0.18
Atg2 / M-Ol	0.21	0.17	0.14	0.09
K_D Atg/Ol from bibliography				
	0.45-0.35		0.18	

K_D Atg/Ol Mg from Evans et al.(2008) and Mn from Trommsdorff and Evans, 1974.